A New PWM CSC-Based Wind Energy Conversion System

By

Zijian Wang

A thesis
presented to Lakehead University in fulfillment of the
thesis requirement for the degree of
Master of Science

Thunder Bay, Ontario, Canada, 2020

Author's Declaration

I hereby declare that I am the sole author of this thesis. This is a true copy of the thesis, including any required final revisions, as accepted by my examiners.

Abstract

In order to eliminate the bulky and costly offshore substation, a new offshore wind farm configuration has recently been proposed: series-connected configuration. Among the series-connected configurations, the pulse width modulation current source converter (CSC)-based one is considered a good candidate. In this thesis, a new PWM CSC-based wind energy conversion system is proposed for the series-connected wind farms. Compared with the previous work, the proposed topology reduces the cost and the manufacturing pressure of the system. A new control scheme is proposed to solve the voltage and current imbalance problem of the proposed configuration. In addition, the optimal modulation scheme is investigated for the series-connected CSCs. Simulation results are provided to assist in the investigation and verify the performance of the proposed configuration and control schemes.

Acknowledgments

I would like to express my sincere gratitude to my supervisor, Dr. Qiang Wei for providing his invaluable guidance, comments, and suggestions throughout the course of the project.

To all relatives, friends, and others who in one way or another shared their support morally, financially and physically, thank you.

Table of Contents

List of Figures

List of Tables

List of Symbols

Symbol	Meaning
V_{c1}, V_{c2} … V_{c6}	input capacitor voltages of the modular MFT converter
v_a	grid phase voltage
V_{in}	total input voltage of the modular MFT converter
v_{dc1}, …v_{dcm}	instantaneous input voltage of each CSC
V_{sd}, V_{sq}	*d*- and *q*-axis components of the grid voltage
V_{sd}, V_{sq}	*d*- and *q*-axis components of capacitor voltages
I_{dc}	dc-link current of the offshore wind farm
i_w	converter output PWM current
I_{dc_ge}	generator-side converter determined dc-link current
I_{dc_gr}	grid-side converter determined dc-link current
i_{sd}, i_{sq}	*d*- and *q*-axis components of the grid currents
i_{cd}, i_{cq}	*d*- and *q*-axis components of the capacitor currents
P_g	grid-side active power
Q_g	grid-side reactive power
L_{dc}	dc-link inductance
L_f	grid-side equivalent line inductance
C_f	CSC output filter capacitance
m_a	modulation index of CSC
f_{sw}	switching frequency
f_{sp}	sampling frequency
θ	angle of a vector in the space vector plane
ω	fundamental angular frequency of CSC output current
T_s	sampling period

List of Abbreviations

Abbreviation	Meaning
PWM	pulse width modulation
MV	medium voltage
LV	low voltage
HVAC	high voltage ac
HVDC	high voltage dc
LFT	low frequency transformer
MFT	medium frequency transformer
VSC	voltage source converter
LCC	line commutated converter
CSC	current source converter
TPWM	trapezoidal pulse width modulation
SVM	space vector modulation
SHE	selective harmonics elimination
MPPT	maximum power point tracking
THD	total harmonics distortion
SQ1	sequence 1
SQ2	sequence 2
SQ3	sequence 3
SQ4	sequence 4
SQ5	sequence 5
SQ6	sequence 6
PF	power factor
UPF	unity power factor
PU	per unit

Chapter 1
Introduction

Offshore wind energy is continuously being developed because of its environmental-friendly characteristic and most importantly, the abundant, rapid, and stable offshore wind resources [1]. As of 2019, the total installed capacity of the world is about 29.1 gigawatts (GW), of which 6.1 GW was installed mostly in PR China, United Kingdom, and Germany [2].

For long-distance offshore wind power systems, high voltage DC (HVDC) is the most suitable transmission system. The current offshore wind farm configuration is mainly parallel configuration, which has been put into use by ABB, Siemens, and other companies [3-4]. However, the parallel configuration faces the problems of high cost and complexity as well as low reliability and efficiency [7-9]. Researchers have proposed a series-connected configuration [7-10, 13-16], which can greatly improve the above problems, but this is an emerging technology with technical challenges in power converter topologies and controls.

In this thesis, a new power converter topology for series-connected wind farm configuration is proposed. Innovative control systems are proposed, and optimal modulation schemes are studied. The new topology not only reduces the cost of the system, but also improves flexibility, stability, and efficiency of the system.

This chapter starts with the structure of the offshore wind farm, and then introduces transmission systems, wind farm configurations, and existing power converter topologies proposed for the series-connected wind farm configuration. In addition, the technical challenges of the series-connected configuration are analyzed, and dissertation objectives are proposed.

1.1 Overview of the offshore wind energy conversion systems

Fig. 1-1 shows the basic structure of a typical offshore wind energy conversion system. The fundamental components include wind turbines, generators, offshore converters, transmission cables, offshore and onshore substations. Wind energy is converted into mechanical energy by wind turbines and then converted to electrical energy by generators. After generators, there are offshore converters and step-up transformers. The generated power is transferred from the offshore to the land by the

transmission cables, and then connected to the grid through transformers in the onshore substation. There are two configurations of offshore wind farms, parallel configuration and series-connected configuration. The parallel-connected configuration is a mature technology. However, a bulky and costly offshore substation is required. The series-connected configuration can eliminate the offshore substation, which greatly reduces costs, but it is an emerging technology with technical challenges in topology and control. There are two types of transmission systems, HVDC and high voltage AC (HVAC). For transmission distances greater than 50km, HVDC is the better choice.

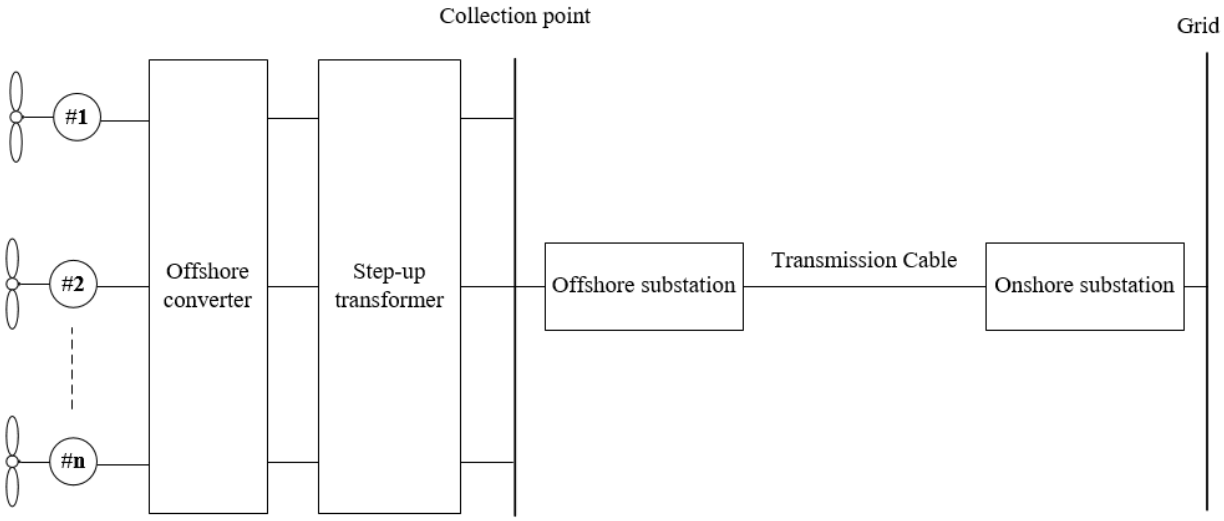

Fig. 1-1 Basic structure of a typical offshore wind energy conversion system.

1.2 Transmission systems

There are two types of transmission systems that can transmit power from offshore wind farms to onshore grid connection points: HVAC and HVDC. The comparison between them is shown below:

1) Cost: The cost of HVDC transmission lines is lower than the cost of HVAC lines. DC transmission requires fewer conductors than AC transmission (2 conductors per DC circuit and 3 conductors per three-phase AC circuit). However, the power converters in HVDC are more expensive than those in HVAC. Therefore, if the transmission distance is higher than 50 kilometers, HVDC costs less, and if the transmission distance is lower than 50 kilometers, HVAC is the more economical option [5].

2) Efficiency: There is no skin effect in DC. Similarly, in the case of direct current, the corona loss is lower. Compared with HVAC, HVDC lines have lower losses over longer distances.

3) Asynchronous interconnection: The AC grid is standardized to 50 Hz in some countries/regions and 60 Hz in other countries/regions. It is impossible to interconnect two AC power grids operating at different frequencies [6]. HVDC can do it.

4) Reactive power compensation: The equivalent capacitance of the AC cable will generate reactive power when carrying current. When the frequency increases or the distance increases, the current carrying capacity of the AC cable decreases. Therefore, reactive power compensation is required at long distances. DC systems do not have this problem.

Overall, HVAC is a more economical option for short transmission distances. When the distance increases, HVDC is the better option.

1.3 Offshore wind farm configuration

Based on the connection methods of wind turbines, there are mainly two types of configurations for offshore wind farms: parallel-connected configuration and series-connected configuration.

1.3.1 Parallel-connected configuration

The structure of the parallel-connected configuration is shown in Fig. 1-2, where the outputs of generator-side power converter are boosted through respective step-up transformers and then connected to the collection system. Then, the collection system is converted to HVDC by another step-up transformer and an HVDC power converter. The second-stage step-up transformer and the HVDC converter are held in the offshore substation. The generated power is transmitted to onshore via the HVDC transmission system, converted to HVAC through an inverter, and then connected to the grid through transformers.

The parallel configuration is a mature solution. ABB's "Bolwin1", "Dolwin1" and "Dolwin2" offshore substations have been put into use in Germany and "Dowin5" and "Dogger Bank" are also expected to be commissioned in Germany and the United Kingdom by 2024 [3]. Siemens will also provide 14 MW Gamesa Turbines for the US Dominion Energy Coastal Virginia Offshore Wind (CVOW) commercial project [4].

However, the offshore substation is very bulky and costly. Fig. 1-3 shows the offshore substation used in "Dolwin2". The complete platform weighs approximately 23,000 tons, is approximately 100 meters long, approximately 70 meters wide, and approximately 100 meters high [3].

In addition, the efficiency and reliability of the parallel-connected configuration is low, and the complexity is high. As shown in Fig. 1-2, the configuration is a multi-stage power conversion system, and therefore the efficiency of the system is low since each stage of power conversion has power losses. Furthermore, the system involves the use of huge amounts of components, which increase the complexity of the system as well as lowering the reliability.

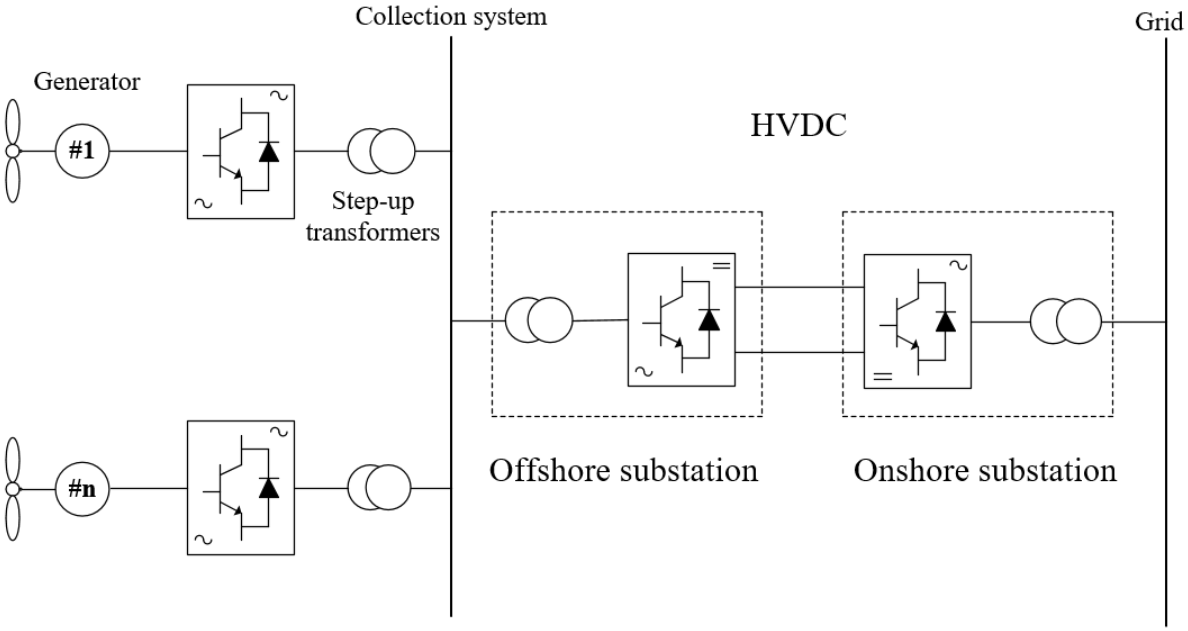

Fig. 1-2 Parallel-connected wind farm configuration.

Fig. 1-3 “Dolwin2" offshore substation [3].

1.3.2 Series-connected configuration

In order to reduce costs and improve the efficiency and reliability, researchers have proposed a new wind farm configuration: series-connected configuration [7-19]. As shown in Fig. 1-4, the outputs of generator-side power converters are connected in series to reach the HVDC level without using any step-up transformers and HVDC converters. Therefore, the bulky and costly offshore substation, step-up transformers and HVDC converters are eliminated, which greatly reduce the costs. In addition, compared to the parallel configuration, the series-connected configuration has a simpler structure with fewer power conversion stages and a smaller number of components. Therefore, the complexity is reduced, and the efficiency and reliability are increased [8]. In summary, the series-connected configuration sees significantly advantages in terms of cost reduction, efficiency and reliability improvement, and is therefore a good candidate for next-generation offshore wind energy conversion systems.

However, the series-connected configuration is an emerging technology. It has not been well studied and technical challenges exist. For example:

1) Generator insulation. Different wind turbine-generator-converter systems have different insulation requirements due to their different distances to the grounding point [7-9]. As shown in Fig. 1-4, the generator furthest from the grounding point has an insulation requirement of an HVDC level. This is not feasible for the generator manufacturing, and so practical insulation methods must be established.

For example, shown in Fig. 1-4, low-frequency transformers are employed between turbines and generator-side power converter to withstand the high voltage stress, and then the generator insulation issue is solved. However, this is not favourable for offshore wind applications since the transformer is very bulky [7].

2) Power converters and controls. Existing power converters and controls which are used in parallel-connected configurations cannot be used here directly. New power conversions and controls should be developed for the series-connected configuration.

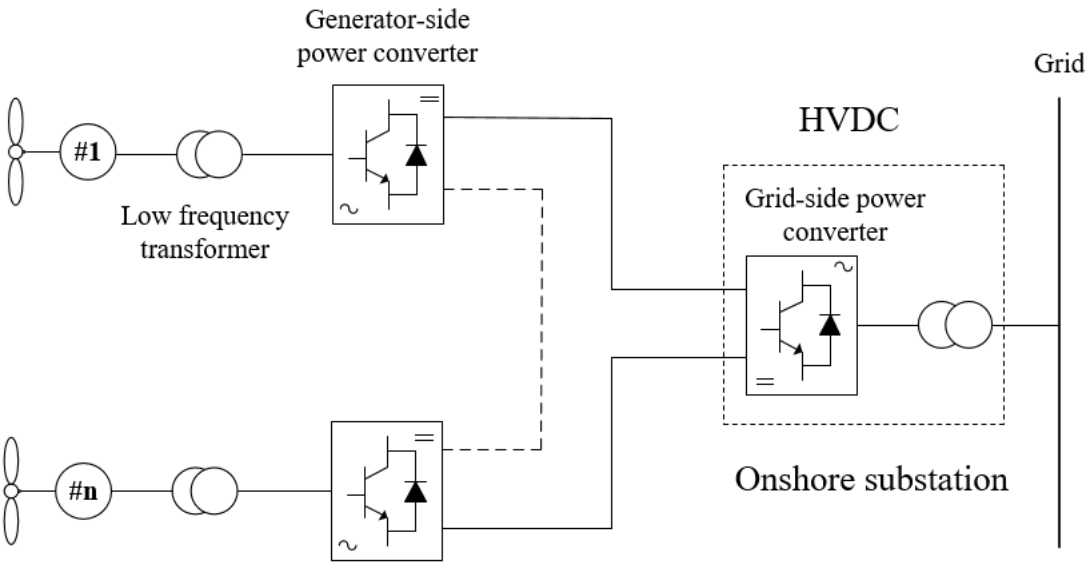

Fig. 1-4 Series-connected wind farm configuration.

1.4 Power converter topology

The available power converter topologies for the series-connected configuration are mainly divided into three types: conventional line commutated converter (LCC), voltage source converter (VSC), and pulse width modulation (PWM) current source converter (CSC).

1.4.1 Conventional line commutated converter-based wind system

Fig. 1-5 shows the LCC-based wind system where series-connected LCCs are employed at both offshore and onshore. The LCC-based topology has been used on land for more than 50 years. However, it has several limitations for offshore wind systems [20-21]: 1) LCC needs a strong grid voltage to assist the commutation of thyristor valves, so LCC is susceptible to grid interference, 2) LCC requires large filters to reduce low-order harmonics, which increases the cost and volume, and 3) LCC cannot provide independent control of active and reactive power, which means that the dc-link current control and power factor control cannot be performed. These limitations make LCC unsuitable for offshore wind power applications.

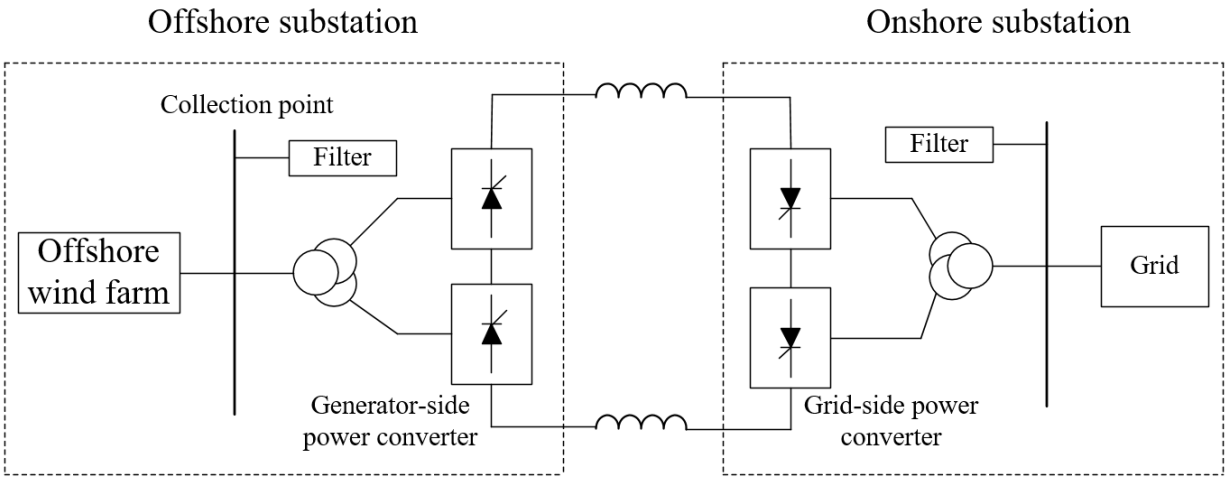

Fig. 1-5 Structure of the LCC-based topology [20].

1.4.2 Voltage source converter-based wind system

The VSC-based topology is the mainstream choice in the parallel configuration-based wind farm and has been implemented into practice. The structure of VSC-based topology for the series-connected configuration is shown in Fig. 1-6. The modular multilevel converters are typically used as the grid-side power converter [22-23], while the generator-side converter can be either a 2-level VSC or a 3-level VSC [23]. The generator-side VSCs convert the collected power from AC to DC and then the power is transmitted from offshore to onshore through HVDC cables. The grid-side VSC converts the DC back to AC and then connected to the grid through transformers. Compared to LCC-based

topologies, the switches used in VSCs have a self-commutated ability and therefore can provide active and reactive power control.

However, VSC-based series-connected configuration have a technical challenge: the DC-link voltage of the VSC-based wind system must always be a constant to ensure grid connection. Shown in Fig. 1-6, when one or some of the generator-side VSCs encounter unexpected failures and has to be bypassed, the DC-link voltage must be controlled as a constant to ensure a continued grid connection. By doing so, the constant DC-link voltage will be evenly distributed to the rest of healthy VSCs, which will cause overvoltage and induce safety issues. To avoid this problem, a redundancy design is required. The voltage ratings of VSCs should be increased or more back-up VSCs should be connected in series, but both methods increase the cost.

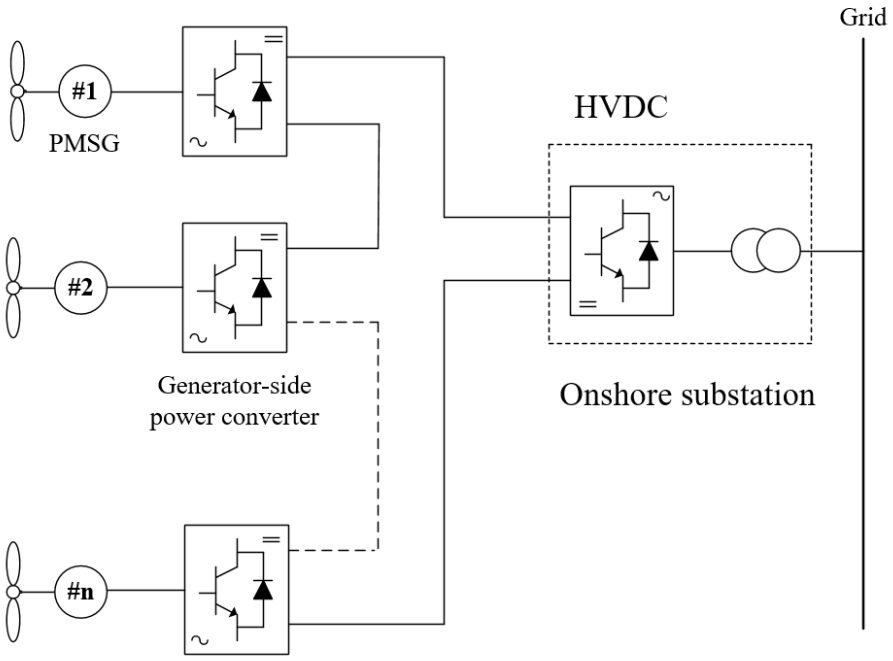

Fig. 1-6 Structure of the VSC-based topology [22].

1.4.3 PWM current source converter-based wind system

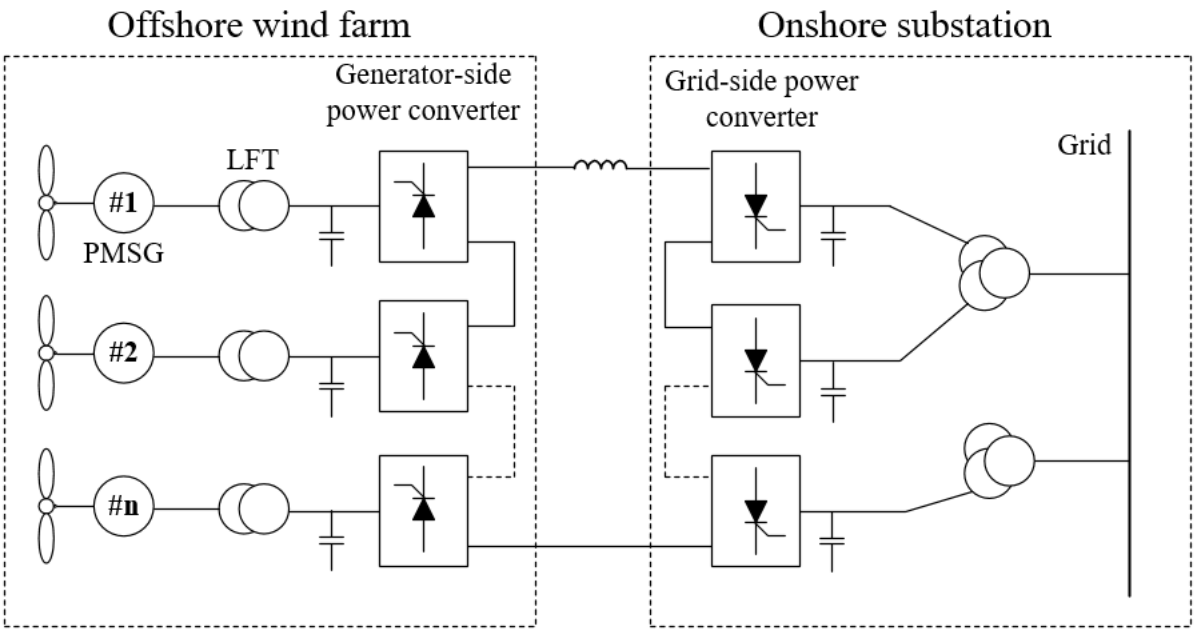

Fig. 1-7 Structure of the CSC-based topology [9].

Fig. 1-7 shows the PWM CSC-based wind system. Compared to the LCC-based system, this one has self-commutated ability and can provide independent active and reactive power control. Compared to the VSC-based one, this system does not have the constraint of a constant DC-link voltage under any conditions and is therefore a good candidate for the series-connected wind system. As shown in Fig. 1-7, even if some generator-side CSCs encounter a bypass due to whatever reasons, there is no overvoltage on the healthy CSCs. This is because the DC-link voltage of the CSC-based system is not a constant. Instead, it is variable and ranges from 0 to 1 per unit (pu) in the full operation range. The voltage stress of generator-side CSCs is only related to the power generated by the connected generator. Similarly, the voltage across each grid-side CSC will not be affected by fault bypass since it is clamped by the grid voltage. In addition, PWM CSCs have reliable short-circuit protection [28]. To sum up, the PWM CSC-based system is a promising system for the series-connected wind energy conversion systems.

The grid-side power converter of the PWM CSC-based system shown in Fig. 1-7 is constructed by connecting identical CSCs in series at input and in parallel at output through multi-winding transformers. For the generator-side power converter, different topologies have been proposed [7-9].

Fig. 1-8 shows a traditional PWM CSC proposed for MV turbine systems [9]. This PWM CSC-based generator-side converter features all advantages of a PWM CSC, such as simple topology and good harmonic performance. However, the weight and size suffer because low-frequency transformers (LFT) need to be used to solve the issue of generator insulation as shown in Fig. 1-7.

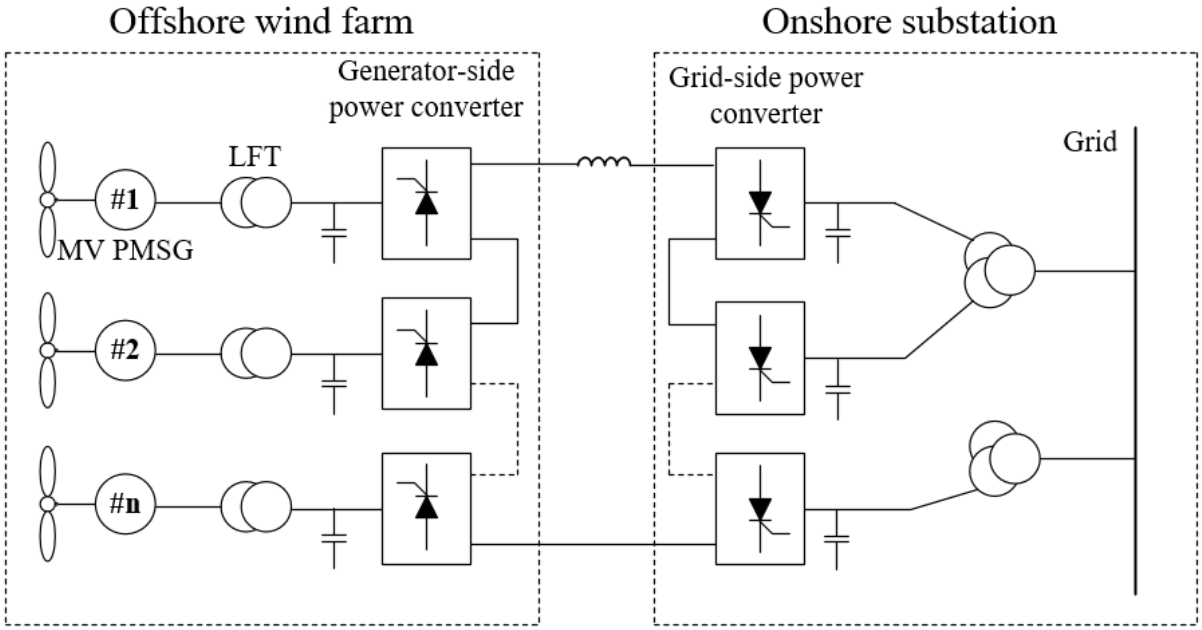

Fig. 1-8 LFT-based generator-side power converter [9].

To keep all advantages of PWM CSCs without introducing extra burden on size and weight, two types of MFT-based generator-side power converters were reported: one is for low-voltage (LV) turbine systems as shown in Fig. 1-9 and the other for MV turbine systems as shown in Fig. 1-10.

Shown in Fig. 1-9, the MFT-based generator-side power converter consists of a LV (690 V) turbine connected to a permanent magnet synchronous generator (PMSG), a low-cost three-phase diode rectifier, and an MFT-based modular converter [8]. The MFT-based modular converter is composed of a couple of LV converter connected in parallel at input and in series at output. Such a structure enables the use of MV PWM CSC at the grid-side of the system and therefore all advantages of PWM

CSCs are inherited. In addition, compared with LFT-based converter shown in Fig. 1-7, the MFT-based one sees smaller size and weight as well as a higher reliability due to the adoption of a modular design.

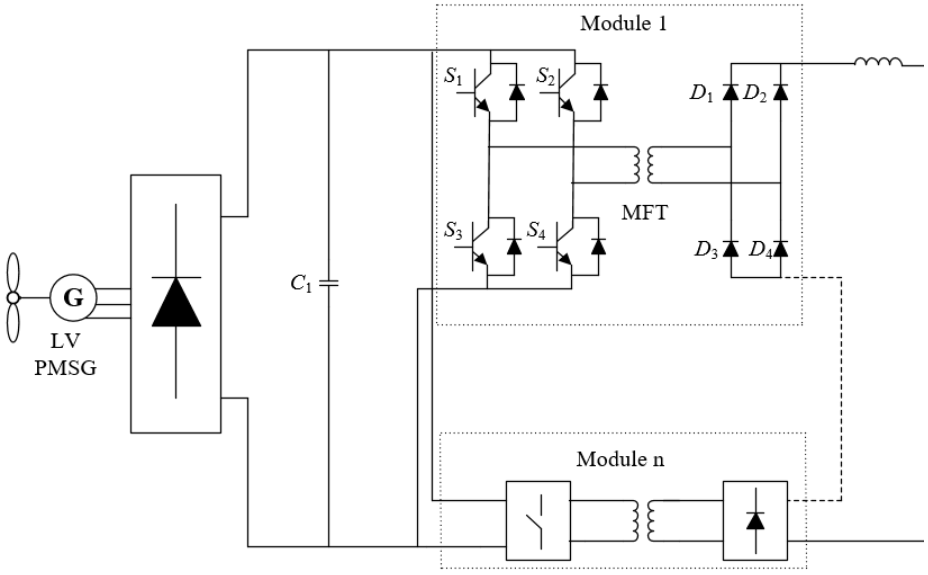

Fig. 1-9 MFT-based generator-side power converter for LV turbine systems [8].

Fig. 1-10 illustrates the MFT-based generator-side converter proposed for the MV turbine systems [7]. It includes an MV turbine-PMSG, a low-cost three-phase diode rectifier, and an MFT-based modular converter. The MFT-based modular converter has a different structure in comparison with that in the LV turbine system shown in Fig. 1-9. The constituent converters are connected in series at both input and output. By dosing so, the low-voltage switches with a lower cost can be used for MV turbine systems. As well, a smaller size and weight and a higher reliability are expected compared with the LFT-based one.

However, the MFT-based generator-side power converter proposed for MV turbine systems has a couple of challenges:

1) The use of low-cost switches at higher power ratings. As the power rating of each turbine system increases, high-current switches are required. These high-current switches however are expensive.

2) Practical manufacturing of high-power MFT. As the power rating of each turbine system increases, the power each MFT carries increases. However, high-power MFT with high-voltage insulation requirements are not mature.

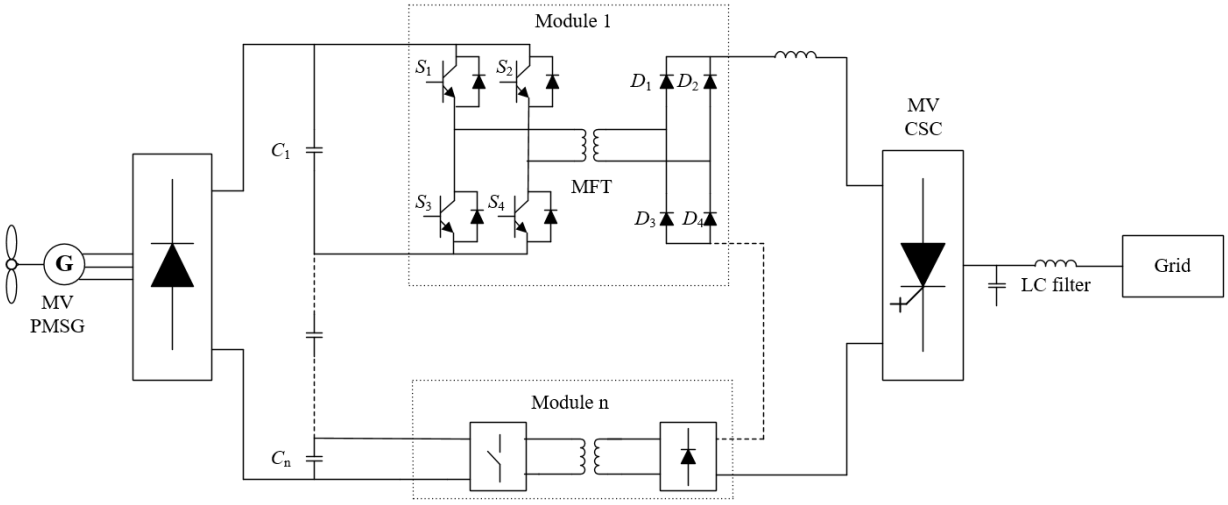

Fig. 1-10 Proposed MFT-based configuration in [7] for MV systems.

1.5 Dissertation objectives

As mentioned earlier, the PWM CSC-based series-connected configuration is a promising solution for next-generation offshore wind farms. And the MFT-based power converter with potential advantages of smaller size and weight and higher reliability is a good candidate for the generator-side power converter of the series-connected system. However, in the application of high power MV turbine systems, it suffers from two technical challenges as the power rating increases: one is the use of expensive switches and the other the need of immature high-power high-voltage MFTs.

Therefore, this thesis is dedicated to reducing the cost of generator-side power converters and the manufacturing burden on the MFTs A new topology will be proposed for the generator-side power converter of the PWM CSC-based series-connected wind system. In addition, optimal modulation schemes will be studied for the proposed new power converter.

The main objectives of this dissertation will be summarized as follows:

1) New generator-side power converter with lower cost and easier manufacturing

A new generator-side power converter will be proposed for the PWM CSC-based series-connected wind system. The cost of the converter is lower by using more cost-effective switches. Besides the burden on the MFTs manufacturing is reduced by a proper design.

2) Optimal modulation scheme investigation for the grid-side PWM CSCs

All modulation schemes for the grid-side CSCs will be investigated and compared, based on which the optimal modulation scheme will be selected for the series-connected CSCs.

Chapter 2

A New PWM CSC-Based Series-Connected Offshore Wind Energy Conversion System

As discussed in the previous chapter, the MV (2.4-69 kV) generator-side power converter of the PWM CSC-based has two technical challenges: the use of expensive high-current switches at higher power ratings, and immature manufacturing of high-power MFT. Therefore, the objective of this chapter is to propose a new PWM CSC-based wind energy conversion system to address the above two problems.

This chapter first introduces the proposed new PWM CSC-based wind energy conversion system. The operation principle of the proposed power converter including both generator- and grid-side power converters is thoroughly illustrated and analyzed. On this basis, a control strategy is proposed. Finally, simulation results are provided to verify the performance of the proposed power converter and control.

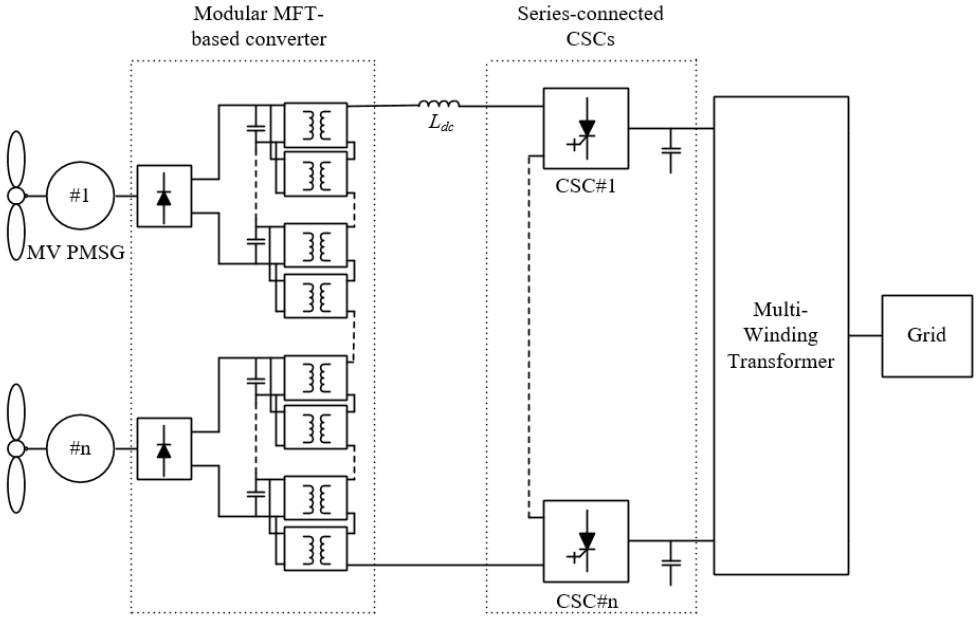

Fig. 2-1 Proposed PWM CSC-based series-connected offshore wind farm.

2.1 Proposed PWM CSC-based wind energy conversion system

Fig. 2-1 shows the configuration of the proposed PWM CSC-based series-connected offshore wind energy conversion system. This conversion system includes two subsystems: offshore conversion system and onshore conversion system. In the offshore part, a few wind energy conversion systems are connected in series to form an HVDC. Each wind energy conversion system consists of a turbine, an MV generator, and a generator-side MFT-based power converter. In the onshore part, multiple CSCs are connected in series to form grid-side power converters of the wind system, and then connected to the grid through a multi-winding transformer. A DC-link inductor is used and connected between power converters at the two parts to enable a continuous and smooth DC current of the PWM CSC-based wind system.

The control of the offshore and onshore subsystems is decoupled. In addition, all generator-side power converters in the offshore subsystem are designed to be identical and independent in control. The same is true for the grid-side power converters. Therefore, in this chapter, one turbine-based conversion system will be taken as an example to illustrate the proposed power converter and control.

2.1.1 Generator-side converter

Fig. 2-2 shows the topology of the generator-side power converter of the proposed wind system. It consists of an MV PMSG, a three-phase diode rectifier, and a modular MFT-based converter. The three-phase diode rectifier has the advantages of high reliability, low cost, low size and weight. However, the diode rectifier generates a relatively high torque ripple in the generator [7]. The synchronous inductance of a PMSG is usually around 25 mH which helps reduce the torque ripple [27]. The modular MFTs as discussed earlier are to address the issue of the generator insulation. Overall, the generator-side converter has two functions: generator speed control and generator insulation problem solving.

A. Operation principles

Shown in Fig. 2-2, the MFT-based modular converter is with a hybrid configuration with H-bridge converters connected in both series and parallel at input and in series at output. The series- connection of n converters at input can reduce the input voltage of each H-bridge converter which enables the use of low-voltage switches, and the parallel-connection of the m converters can reduce the average current of each converter which enables the use of low-current switches. In addition, the series-connection of such n*m converters at output can increase the voltage gain of the generator-side

converter which facilitates the construction of HVDC using less turbine units. The numbers, n and m, are determined by the voltage and current ratings of each turbine system as well as the used switches.

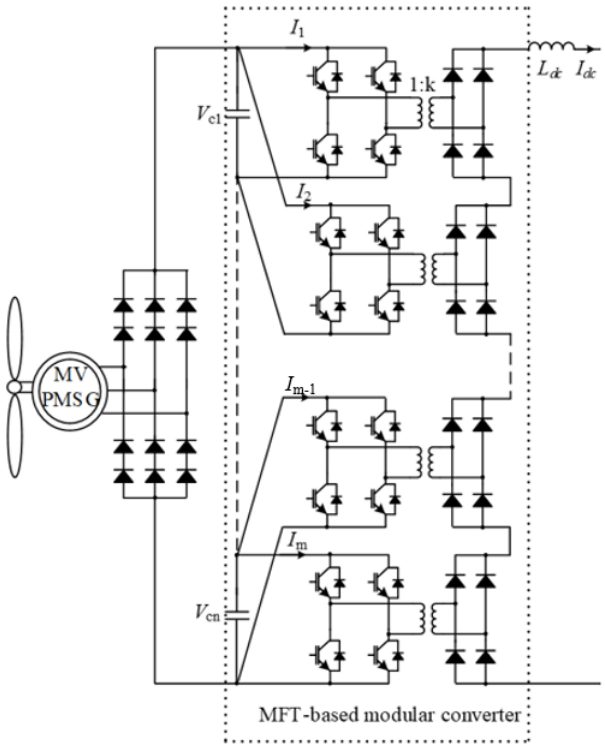

Fig. 2-2 Proposed generator-side MFT-based modular converter.

For example, in the previous study [7] where 20 pieces of 1700V/400A IGBTs are needed for a 4000V/1MW turbine system, while in the proposed converter, 40 pieces of 1700V/200A IGBTs are required by the use of 10 H-bridge converters with 5 in series connection and 2 in parallel connection (2 converters share one capacitor as shown in Fig. 2-2). Though the number of switches as well as their drivers, and diodes are doubled, the finalized cost of the proposed converter is lower because the price of such switches with twice the rated current ratings are more than doubled. For the case of turbine systems with megawatts level, such as 4000V/2MW, a lower cost of the power converter can be expected by either 1) further doubling m so that 1700V/200A IGBTs can continue to be used, or 2) maintaining the current m, while using the 1700V/400A IGBTs, whichever is cheaper. For the final design, a comprehensive evaluation including the cost of switches, drivers, and diodes should be conducted.

B. Modular medium-frequency transformer

The modular MFTs are introduced in the proposed topology mainly to solve the problem of generator insulation. Besides, the MFT can help realize zero-voltage switching (ZVS) for the primary switches through its leakage inductance without requiring additional components [7-8, 15].

In the series-connected configuration, the turbine-generator furthest from the grounding must withstand an HVDC level [7], and therefore insulation must be accomplished. Some of the following approaches can be used for generator insulation [9]: 1) Establish insulation between the generator winding, filter capacitor and CSC 2) Isolate the wind turbine and maintain the nacelle; and 3) Transformer-based insulation method. Among them, the transformer-based solution is considered the most feasible. Compared with the bulky LFT, MFT has a smaller size and weight, which is important for offshore wind power applications. The high-power MFT with high-voltage insulation levels is immature, and the main technical challenges are:

1) Thermal and cooling system design. With an increased frequency, the increased losses (hysteresis, eddy current, copper) and reduced volume cause strict challenges to the thermal design [24-26].

2) Insulation design. In the series-connected wind farm configuration, the maximum insulation level of the MFT is the HVDC level. In addition, as the power rating of each turbine system increases, the power each MFT carries increases. A combination of high power and high voltage insulation requirement leads to a burden on the implementation of the MFTs [24-26].

In this proposed power converter, by connecting modules both in series and parallel, each MFT carries less power compared with that in previous studies [7]. For example, for each generator-side power converter with a power rating of 4000V/1MW, the power of each MFT in the previous study is 0.2MW [7], while it is reduced to 0.1MW in the proposed converter. The burden on MFT manufacturing is therefore reduced.

C. Modulation

The modules in the modular converter are identical, and their control schemes are also identical. Here, the Module 1 shown in Fig. 2-3 is used to illustrate the modulation scheme of the modular converter. The modulation scheme of a single module is shown in Fig. 2-4. Ignoring the dead time and switching time, each cycle is mainly divided into the following states:

1) When $t < t_0$, S_1, S_4, D_1, D_4 are turned on, and the power is transferred to the load.

2) When $t_0 < t < t_1$, S_1, S_2 are turned on, there is no power transmission.

3) When $t_1 < t < t_2$, S_2, S_3, D_1-D_4 are turned on, and the power is transferred to the load.

4) When $t_2 < t < t_3$, S_2, S_3, D_2, D_3 are turned on, there is no power transmission.

5) When $t_3 < t < t_4$, S_1, S_2 are turned on, and there is no power transmission.

The equivalent circuits for each state are shown in Fig. 2-5.

To sum up, this MFT-based generator-side modular converter has advantages of being able to 1) reduce the cost by using low-voltage and low-current switches for MV high-power wind systems, and 2) facilitate the MFT manufacturing by adopting a hybrid modular configuration.

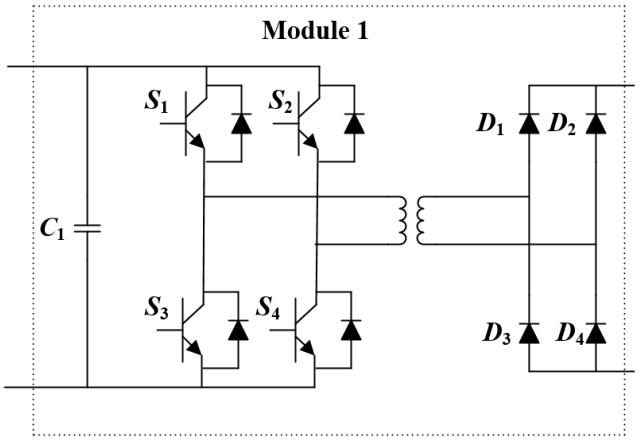

Fig. 2-3 Structure of a single module.

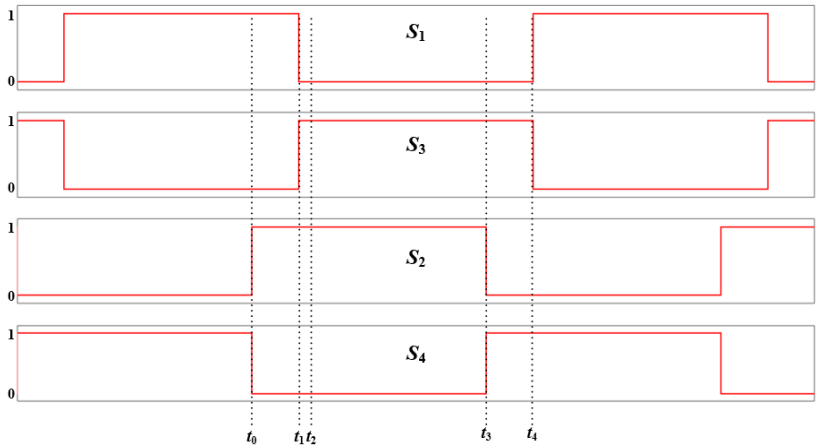

Fig. 2-4 The modulation scheme of a single module.

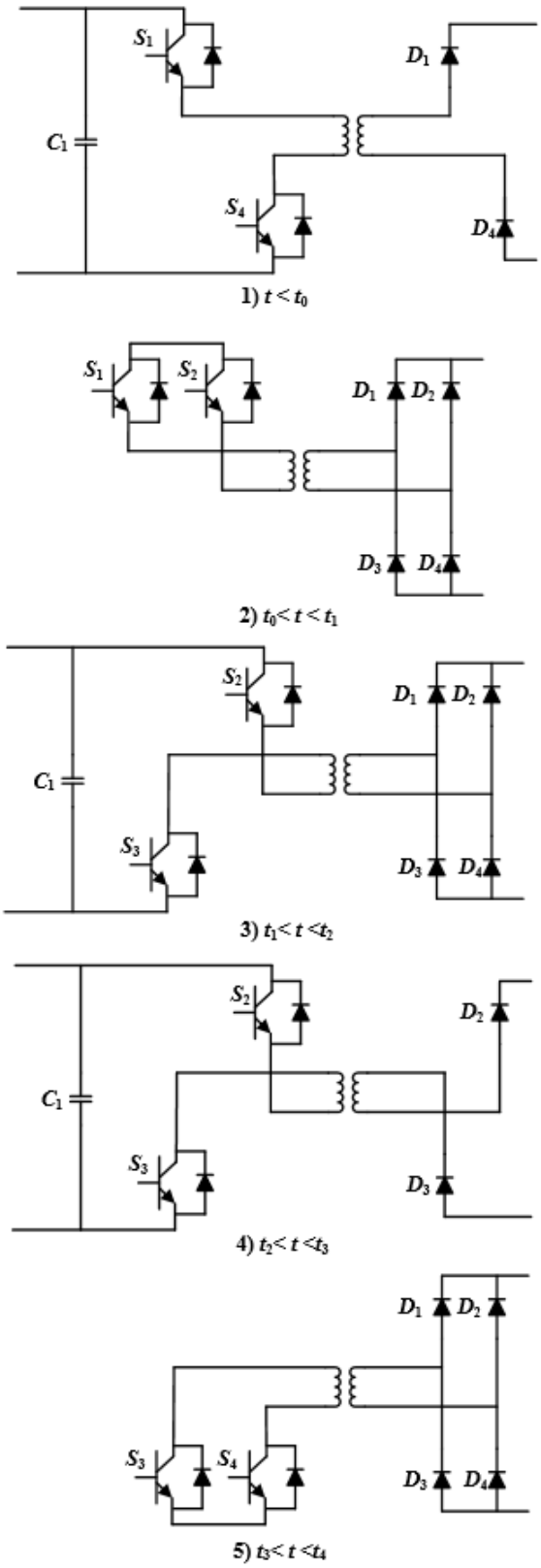

Fig. 2-5 Equivalent circuits for each switching state in Module 1.

2.1.2 Grid-side converter

The grid-side converter is shown in Fig 2-6, in which the offshore part of the proposed wind system is simplified as a DC voltage source V_{in}. Same as that in previous studies [7], a few CSCs are connected in series to function as the grid-side converter of the proposed wind energy conversion system. All CSCs share a same DC-link current. As well, they are designed to be identical and share same gating signals.

Each CSC is connected to an LC filter and then connected to the grid through a multi-winding transformer. The LC filter consists of a filter capacitor C_f and a leaking inductance L_f of the transformer. The functions of LC filters are: 1) reducing the harmonic contents of the current to meet the grid codes, and 2) assisting the switches commutation. Each CSC is composed of six gate-commutated thyristors (GCTs). These GCTs have reverse blocking capability. The switching frequency of these switches is usually set at around 500 Hz to reduce switching losses. Modulation schemes of CSC mainly include space vector modulation (SVM), trapezoidal pulse width modulation (TPWM), and selective harmonics elimination (SHE). Their performance is different and will be introduced in detail in Chapter 3.

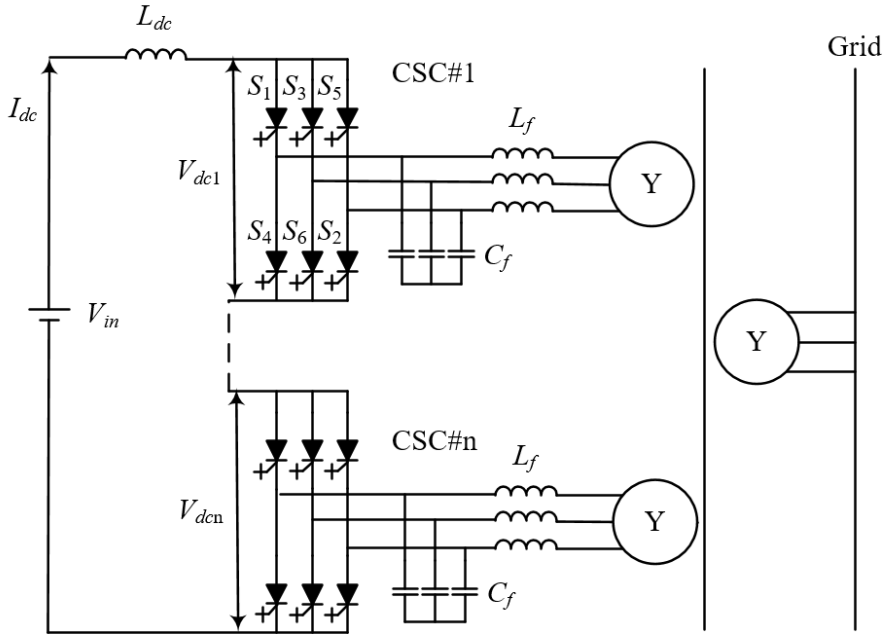

Fig. 2-6 Grid-side series-connected CSCs.

2.2 Control schemes of the converter

Fig. 2-7 illustrates the overall structure of the proposed control schemes. The control schemes for the proposed power converter consists of two parts. One part is the control of the generator-side converters, which includes 1) maximum power point tracking (MPPT); and 2) the balance control of the input current and input voltage of different modules. The other part is the control of the grid-side converters, including 1) DC-link current control, and 2) Reactive power control.

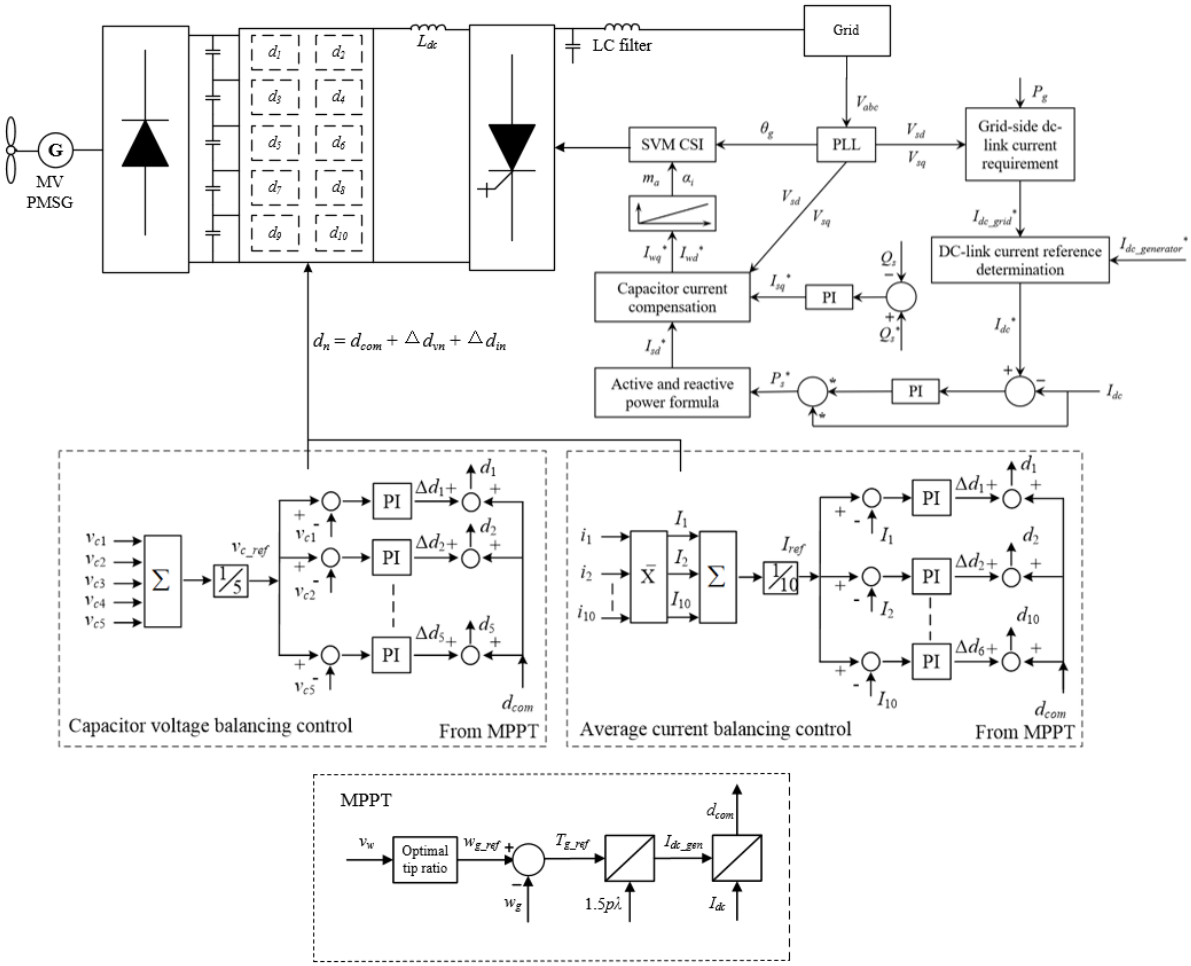

Fig. 2-7 overall structure of proposed control schemes.

2.2.1 Generator-side control

A. Maximum power point tracking (MPPT)

The wind power P_m captured by the blade and converted into mechanical power can be calculated by

$$P_M = \frac{1}{2}\rho A v_w^3 C_p \tag{2-1}$$

where ρ is the power density, A is the sweep area, given by $A = \pi l^2$, where l represents the length of the blade. v_w is the wind speed, and C_p is the power coefficient of the blade.

The main goal of MPPT is maximizing the mechanical power at different wind speeds by maximizing the power coefficient of the blade. The typical MPPT schemes are shown below [1]:

1) MPPT with optimal power control. The power profiles define the maximum power that the turbine can produce at different wind speeds. The generated power is sent to the generator control system, which compares the power reference with the power sent from the generator to generate a control signal for the power converter.

2) MPPT with optimal speed control. The measured wind speed is used to generate the generator speed reference value based on the best tip speed ratio, and the generator speed is controlled by the power converter.

3) MPPT with optimal torque control. For a given gear ratio, the mechanical torque of the turbine can be converted into the mechanical torque of the generator. The generator speed is measured and used to calculate the required torque reference. Through feedback control, the generator torque is equal to the torque reference at steady state.

The scheme of MPPT with optimal generator speed control is used in this thesis as an example. First, considering an ideal condition where components are identical, the MFT-based modular converter is equivalent to a Buck converter. The generator-side converter is then simplified as shown in Fig. 2-8. The real-time wind speed v_w is measured and the optimal generator speed reference w_{g_ref} at this wind speed is generated from the measured wind speed. Then the engine speed w_g is controlled equal to w_{g_ref} by the generator-side converter to achieve MPPT. At this time, the generator generates current I_{dc_gen}, since I_{dc} is controlled by grid-side converters, the ratio of I_{dc_gen} to I_{dc} is the duty cycle d_{com} of the generator-side converter. By applying d_{com} to the modular MFT-based converter, MPPT is achieved.

However, components can not be guaranteed to be identical in practice, such as the turn ratios of the transformers. Using d_{com} at all modules will then cause current and voltage imbalance problems, which will be introduced in the next section.

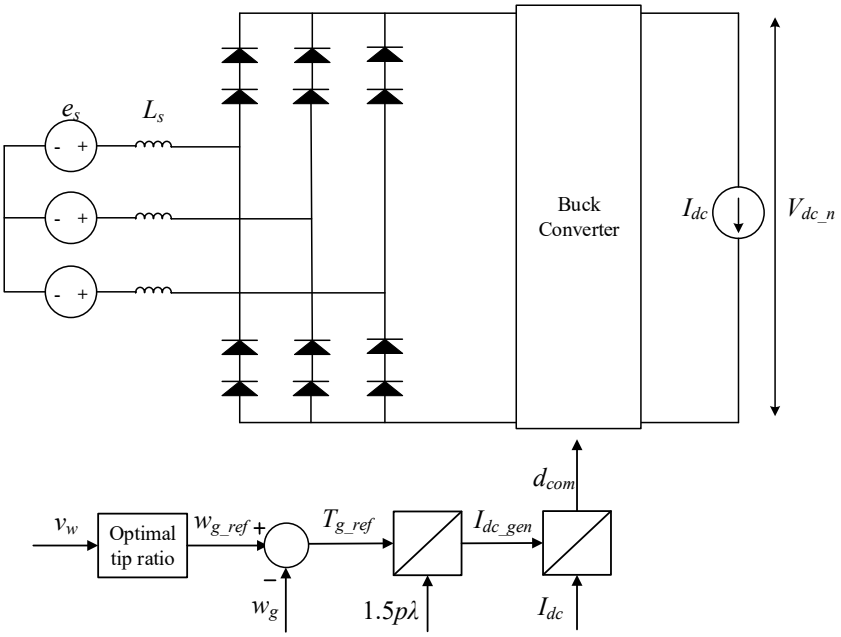

Fig. 2-8 MPPT with optimal generator speed control [15].

B. Voltage and current balance control

The components of the modular converter are designed to be the same, but in practice some parameters cannot guaranteed to be identical. For example, the turn ratios of the MFTs in different modules may be different due to the manufacturing technology. This mismatch will cause the voltage and current imbalance that should be addressed. Otherwise, the reliability of the proposed converter suffers.

1) voltage imbalance and control

Fig. 2-9 shows the structure of series-connected modules. Neglecting the transformer losses, the power at both sides of the transformer in a single module should be equal, that is:

$$\begin{cases} V_{C1}I_1 = V_{out1}I_{dc} = d_1 k_1 V_{C1} I_{dc} \\ V_{C2}I_2 = V_{out2}I_{dc} = d_2 k_2 V_{C2} I_{dc} \end{cases} \tag{2-2}$$

It can be concluded that if modules are controlled with the same duty cycle d_{com}, the module with the larger turn ratio (for example $k_1 > k_2$) tends to absorb higher input current than other modules ($i_1 > i_2$). This is a transient process since the input current of the constituent modules should be equal at steady state. Therefore, the capacitor of a module with a larger turn ratio (k_1) must be discharged more to

compensate for the required current. Compared to a module with a smaller turn ratio, the voltage of the capacitor in this module is lower (v_{C1}<v_{C2}).

The solution is compensating the voltage imbalance of the capacitors by using the PI controller to adjust the duty cycle required by each module. First, find the average value of the input voltages of all modules as a reference. Use this reference value to make the difference to each input voltage of each module respectively, and then generate the voltage compensation duty cycle Δd_{vn} through the PI controller. Add Δd_{vn} to the common duty cycle d_{com}, that is, $d=d_{com}+\Delta d_{vn}$, then the voltage imbalance is compensated. Modules with higher capacitor voltages have higher duty cycles. The physical meaning of this method is that, for modules with high capacitor voltages, their capacitors release more power to the load. Discharging will reduce the capacitor voltage, and regulation will continue until the voltages of capacitors are balanced.

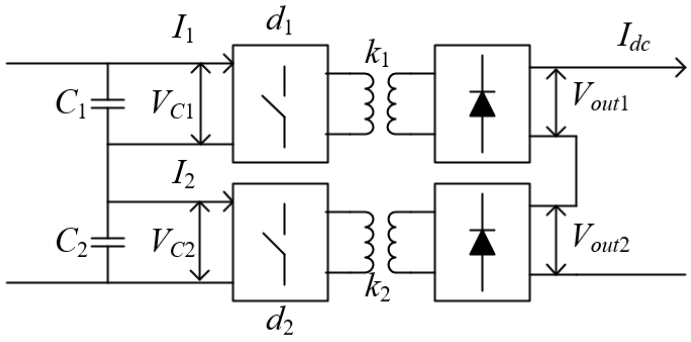

Fig. 2-9 Series-connected modules.

2) current imbalance and control

Fig. 2-10 shows the structure of parallel-connected modules. Since modules connected in parallel share the same input capacitor, the input voltages of the modules are equal (v_{c1} in Fig. 2-10). Neglecting the transformer losses, the power at both sides of the transformer in a single module should be equal, that is:

$$\begin{cases} V_{C1}I_1 = d_1 k_1 V_{C1} I_{dc} \\ V_{C1}I_2 = d_2 k_2 V_{C1} I_{dc} \end{cases} \tag{2-3}$$

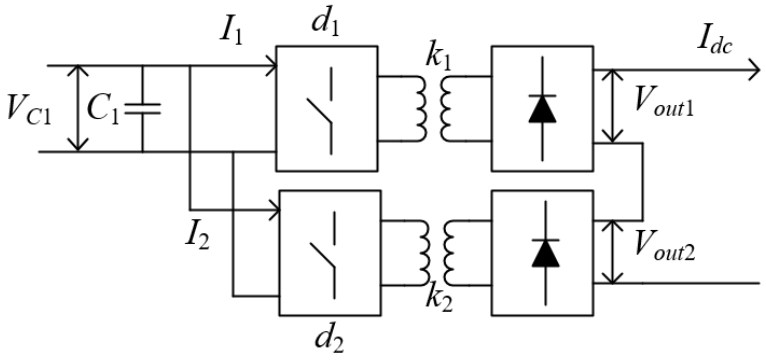

Fig. 2-10 Parallel-connected modules.

The module with a larger turn ratio (for example $k_1>k_2$) will absorb more input current ($i_1>i_2$). This is a transient process since the input current of the constituent modules should be equal at steady state. Therefore, the module with a larger turn ratio (k_1) must transfer less power to the load to reduce its input current.

The solution is to adjust the duty cycle so that modules with a larger turn ratio transfer more power to the load. First, find the average value of the input currents of all modules as a reference. Use this reference value to make the difference to each input current of each module respectively, and then generate the current compensation duty cycle Δd_{in} through the PI controller. Add Δd_{in} to the common duty cycle d_{com}, that is, $d=d_{com}+\Delta d_{in}$, then the current imbalance is compensated.

By adding both compensation duty cycles to d_{com}, the final duty cycles are shown below:

$$d_n = d_{com} + \Delta d_{vn} + \Delta d_{in} \tag{2-4}$$

Then both voltage and current imbalance are compensated by applying (2-4). The complete balance control block diagram is shown in Fig. 2-7.

2.2.2 Grid-side control

The grid-side control includes active power and reactive power control, also known as dc-link current control and power factor (PF) control. The control scheme is shown in Fig. 2-11, composed of two independent control loops for active power and reactive power regulation, respectively.

The grid-connected CSCs can be controlled using various schemes [1]. The voltage-oriented control (VOC) is used here. The control algorithm is implemented in the grid-voltage synchronous

reference frame, where all the variables are of DC components in steady state [27]. Grid voltage phase-locked loop (PLL) is introduced to the control system to obtain synchronous angle θ_g and the angular frequency ω_g. Through *dq* transformation, the *dq* component of the grid voltage V_{sd} and V_{sq} are also obtained.

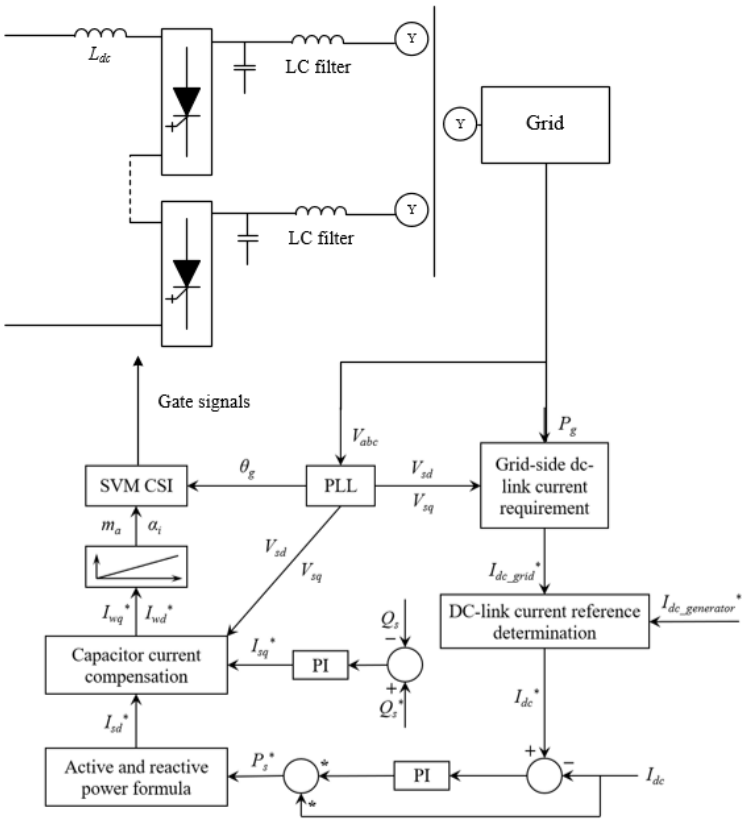

Fig. 2-11 Grid-side control diagram.

The DC-link current refence determination plays an essential role in the control. The CSC can be controlled to be constant, or variable according to the change of input power. A constant DC-link current provides a faster dynamic response, while a variable lower DC-link current greatly reduces system losses [1]. However, in wind energy systems, a fast response is not necessary, while a high efficiency is more preferred. In short, an appropriate "minimum" DC-link current reference is preferred for the proposed CSC-based wind system.

There are two minimum dc-link current references: one is the generator-side minimum current reference and the other the grid-side minimum current reference. The generator-side minimum dc-link reference current is to achieve MPPT while the grid side reference current to achieve required PF

control. The final dc-link current reference of the system should be greater than or equal to the maximum of the two minimum reference currents.

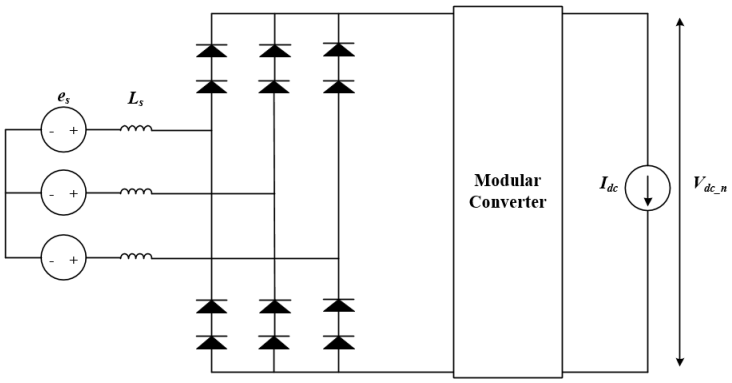

Fig. 2-12 Simplified modular MFT-based converter for unit #n [7].

A. Generator-side minimum dc-link current reference

A simplified modular MFT-based generator-side converter for unit #n is shown in Fig. 2-12. PMSG is simplified to a voltage source (e_s) with a finite source inductance (L_s), and the load on the DC-link is regarded as a current source. The presence of input line inductance causes the current commutation in the rectifier to be not instantaneous and will cause the DC output voltage V_{dc_n} to drop []. The commutation angle and the resulting voltage drop depend on the generator inductance L_s and the DC link current I_{dc}. If the commutation angle is less than 60º, the average DC output voltage V_{dc_n} is:

$$V_{dc\_n} = \frac{3\sqrt{2}}{\pi} E_{s,LL} - \frac{3}{\pi} \omega_s L_s I_{dc} \tag{2-5}$$

where $E_{s,LL}$ is the rms value of the line-to-line back-EMF e_s, w_s is the optimum electrical speed of the PMSG under MPPT. Assume the captured wind power P_{ge_n} is transferred to the DC side power P_{dc_n} with no loss, which is,

$$P_{dc\_n} = V_{dc\_n} I_{dc} = P_{ge\_n} \tag{2-6}$$

In order to achieve MPPT, the synchronous generator needs to meet the constraints:

$$E_{s,LL}{}^2 \geq \frac{2\pi}{3} \omega_s L_s P_{ge\_n} \tag{2-7}$$

Combining (2-5) and (2-6) gives the dc-link reference current:

$$I_{dc\_gen}^{*} = \frac{3\sqrt{2}E_{s,LL} - \sqrt{18E_{s,LL}^{\ 2} - 12\pi\omega_s L_s P_{ge\_n}}}{6\omega_s L_s} \tag{2-8}$$

B. Grid-side minimum dc-link current reference

Shown in Fig. 2-11, the dc-link current can be calculated according to the grid-side active power output P_g, which equals to the generator output power P_s in steady state ($P_s = P_g$). The following formula is used to obtain the required d-axis current of the grid-side converter.

$$\begin{cases} P_g^{*} = V_{dc}^{*} I_{dc} \\ i_{sd}^{*} = \dfrac{P_g^{*}}{v_{sd}} \end{cases} \tag{2-9}$$

The q-axis current reference i_{sq}^{*} can then be obtained from:

$$i_{sq}^{*} = \frac{Q_g^{*}}{-1.5 v_{sd}} \tag{2-10}$$

where Q_g^{*} is the reference for the reactive power, which can be set to zero for unity power factor operation, a negative value for leading power factor operation, or a positive value for lagging power factor operation.

Derive the reference current of the CSI as following formula:

$$\begin{cases} i_{wd}^{*} = i_{sd}^{*} + i_{cd} = i_{sd}^{*} - \omega_g C_f V_{cq} \\ i_{wq}^{*} = i_{sq}^{*} + i_{cq} = i_{sq}^{*} + \omega_g C_f V_{cd} \\ V_{cd} = R_g i_{sd} + V_{sd} - \omega_g L_g i_{sq} \\ V_{cq} = R_g i_{sq} + \omega_g L_g i_{sd} \end{cases} \tag{2-11}$$

With the modulation index m_a being set to its maximum value, that is 1, to lower conduction losses [1], the minimum dc-link current I_{dc_gr} determined by the grid-side converters is shown below:

$$I_{dc\_gr}^{*} = \sqrt{\left\{(1-\omega_g^2 L_g C_f)\left(\frac{2P_g}{3nV_{sd}}\right) - \omega_g R_g C_f \left(\frac{2Q_g^{*}}{3V_{sd}}\right)\right\}^2 + \left\{(1-\omega_g^2 L_g C_f)\left(\frac{2Q_g^{*}}{3nV_{sd}}\right) + \omega_g C_f V_{sd} + \omega_g R_g C_f \left(\frac{2P_g}{3V_{sd}}\right)\right\}^2} \tag{2-12}$$

C. Final dc-link current reference

After calculating the dc-link current reference both on the grid-side and the generator-side separately, take the larger of the two:

$$I_{dc}^{*} = \max(I_{dc\_generator}^{*}, I_{dc\_grid}^{*}) \tag{2-13}$$

By applying the minimum dc-link current reference shown in (2-13), the required control objectives at both generator- and grid-sides are achieved.

2.3 Simulation results

The performance of the proposed topology and the effectiveness of the proposed voltage/current balance control scheme are verified by MATLAB/Simulink. The simulation is divided into three parts. The first part verifies the effectiveness of the balance control through the presence or absence of balance control in different time intervals. The second part simulates the power converter under a step change in the wind speed. The third part verifies the performance of the proposed converter under reactive power control. Note that in the simulation, the turbine-generator is replaced with a variable three-phase voltage source supply. And the performance of the power converter under a stepped wind speeds is simulated by using a stepped change in the source supply. This simplification however is effective to verify the performance of the proposed power converter and control.

Table 2-1 Parameters in Simulation

<table>
<tr><td colspan="2">System Rating</td><td colspan="2">PMSG</td></tr>
<tr><td>Nominal Power</td><td>1MW</td><td>Rated Line-to-Line Voltage (rms)</td><td>4000V</td></tr>
<tr><td>Grid Voltage</td><td>4160V</td><td>Synchronous Inductance</td><td>0.4 p.u.</td></tr>
<tr><td>Frequency</td><td>60Hz</td><td>Stator Resistance</td><td>0.1 p.u.</td></tr>
<tr><td colspan="4">Generator-side converter</td></tr>
<tr><td>Number of modules</td><td>10</td><td colspan="2">Turn ratios of transformers</td></tr>
<tr><td>Input Capacitor</td><td>2.0 p.u.</td><td colspan="2" rowspan="2">1:1; 1:1.1; 1:1.01; 1:1.11; 1:1.02; 1:1.12; 1:1.03; 1:1.13; 1:1.04; 1:1.14</td></tr>
<tr><td>Switching Frequency</td><td>1200Hz</td></tr>
<tr><td colspan="4">Grid-side converter</td></tr>
<tr><td>Switching Frequency</td><td>540 Hz</td><td>DC-link Inductance</td><td>0.6 p.u.</td></tr>
</table>

All parameters used are listed in Table 2-1. Ten modules are employed in the modular MFT-based converter. The turn ratios of the ten transformers are purposely set to 1:1 (Module 1), 1:1.1 (Module 2), 1:1.01 (Module 3), 1:1.11 (Module 4), 1:1.02 (Module 5), 1:12 (Module 6), 1:1.03 (Module 7), 1:1.13 (Module 8), 1:1.04 (Module 9), and 1:1.14 (Module 10) to simulate the performance of the proposed converter under mismatches.

2.3.1 Performance with and without balance control

Figure 2-13 illustrates the simulated performance of the proposed power converter with/without voltage and current balance control under unity power factor (UPF). Fig. 2-13 (a) shows input voltages of the modules (V_{c1}-V_{c5}), noted that every two modules share one input voltage; Fig. 2-13 (b) shows the input currents of the modules (I_1-I_{10}); and Fig. 2-13 (c) shows the dc-link current of the converter (I_{dc}). Before t = 0.5s, the system operates in steady state with voltage and current balance control. The input voltage and input current of each module are balanced. At t = 0.5 s, the balance control is deactivated, and all modules operate at the same duty cycle d_{com}. The input voltages and input currents of the respective modules are imbalanced. At t = 0.5 s, the balance control is reactivated, and input voltages and input currents start to rebalance. I_{dc} remains constant throughout the whole process.

2.3.2 Performance under stepped input voltage

Figure 2-14 illustrates the simulated performance of the proposed converter under stepped wind speeds. As mentioned in 2.2.2, PMSG can be simplified as a voltage source with a finite source inductance, so the stepped wind speed can be simulated by the stepped input voltage of the voltage source. Before t = 0.5s, the equivalent input voltage is 3000V. At t = 0.5s, the equivalent input voltage changes to 4000V, At t = 1s, the equivalent input voltage changes back to 3000V again. Balance control is activated throughout the whole process. Fig. 2-14 respectively shows the input voltages, input currents, and dc-link current of the proposed converter in three stages of changes. It turns out that the proposed power converter and the control scheme can operate successfully under the stepped input.

2.3.3 Performance with reactive power control

Fig. 2-15 shows the simulated performance under reactive power control. By controlling the reactive power Q_s, the PF is set to -0.95, 1, and 0.95, respectively. Fig. 2-15 shows the phase relationship between the phase A injection current i_{SA} and the phase A grid voltage V_A under the three power factors shown above. When PF = -0.95, i_{SA} is leading V_A; When PF = 1, i_{SA} and V_A are in phase; when PF = +0.95, i_{SA} is lagging V_A.

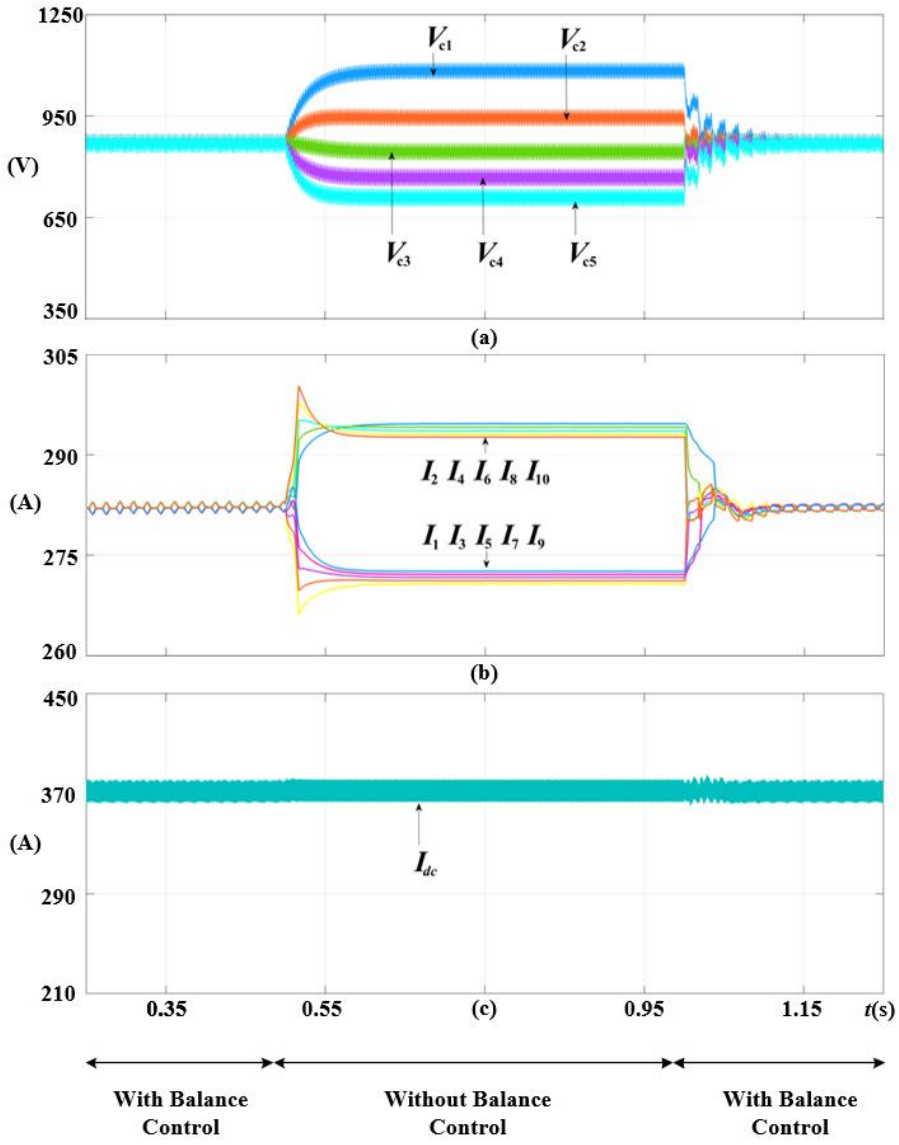

Fig.2-13 Simulated performance with and without balance control.

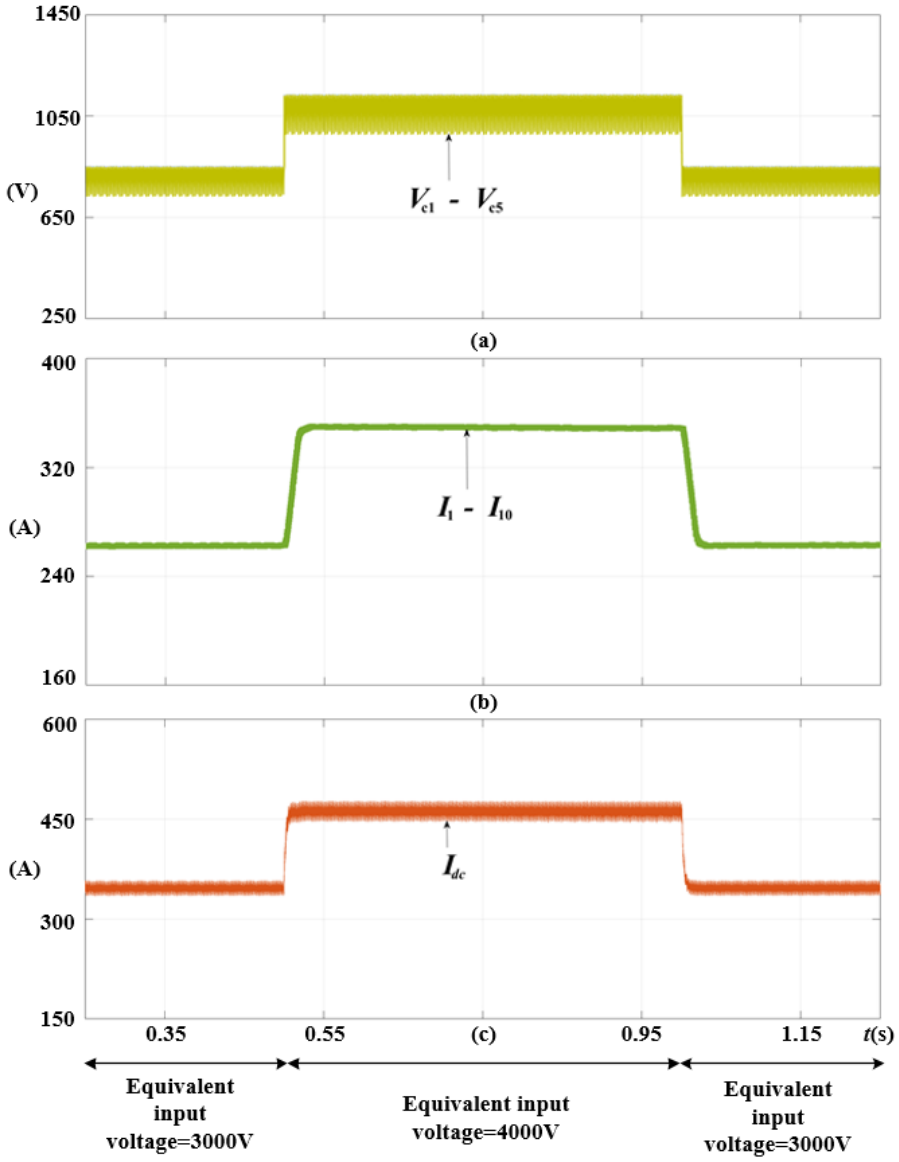

Fig.2-14 Simulated performance under stepped input voltage.

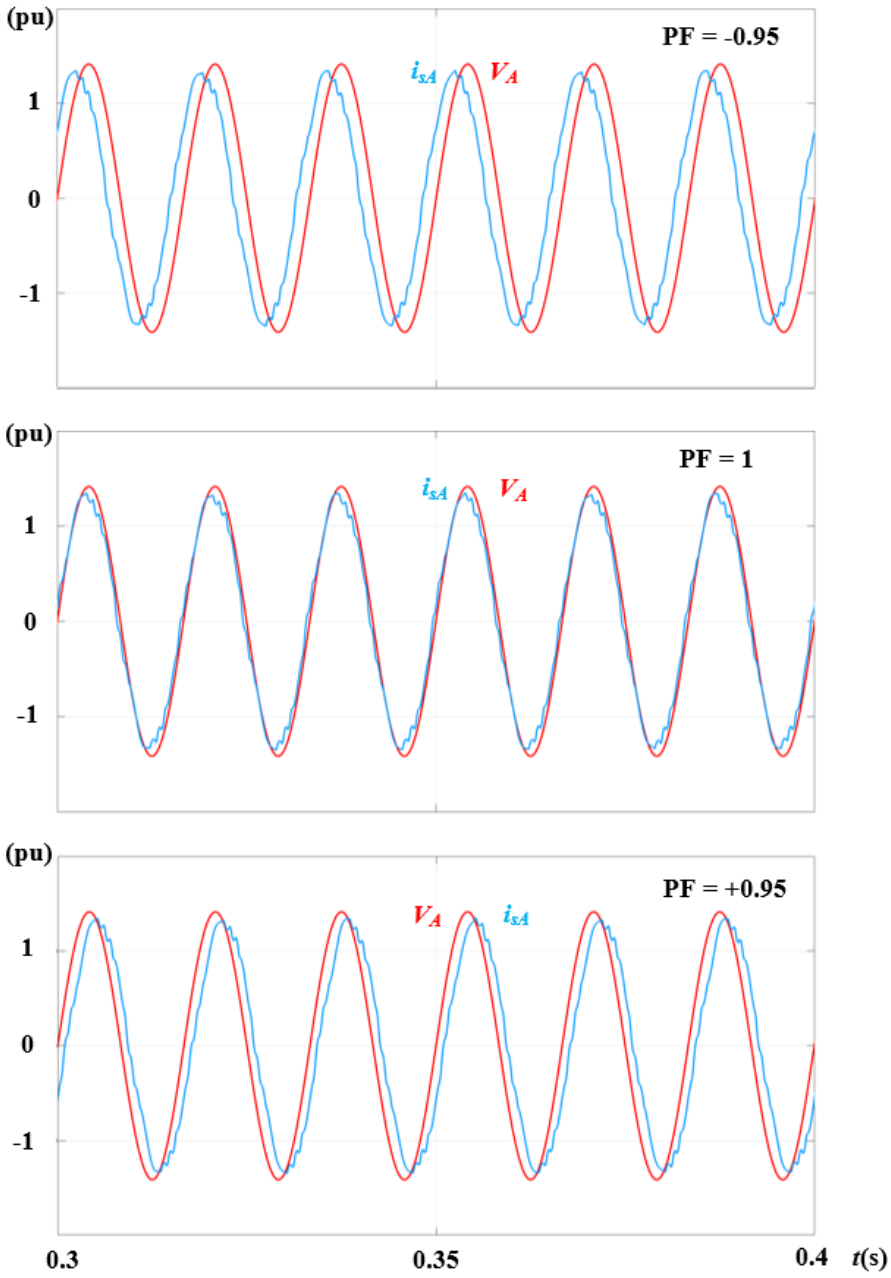

Fig.2-15 Simulated performance under reactive power control.

2.4 Summary

In this chapter, a medium frequency transformer (MFT)-based power converter topology is proposed for the series-connected offshore wind farm configuration. Compared with the previous work, the proposed topology can: 1) reduce the cost by using low current switches, 2) facilitate the construction of HVDC using less turbine units by increasing the generator-side voltage gain, and 3) reduce the burden on MFT manufacturing by reducing the power rating of MFT.

Due to component tolerances of the MFT-based modular converter, the current and voltage among the constituent modules are imbalanced. In order to solve this problem, a voltage and current balance control scheme is proposed. Simulations are performed to verify the performance of the proposed configuration and the effectiveness of the proposed scheme.

Chapter 3

Optimal Modulation Scheme Investigation for Series-Connected PWM Current Source Converters

In the topology proposed in Chapter 2, the grid-side converter is composed of multiple CSCs connected in series. In the series-connected CSCs, the required DC-link inductor is very bulky and costly, and its size is related to the employed modulation scheme. In addition, the DC current utilization, output current harmonics and filter sizing of the CSCs are all affected by the used modulation scheme. Therefore, in this chapter, existing commonly used modulation schemes are investigated, and the optimal one is selected for the series-connected CSCs.

This chapter first introduces the principles of modulation schemes commonly used for CSCs, and then investigates their performance in terms of harmonic performance, dynamic performance, filter sizing and DC-link inductance, respectively. Finally, the performance of investigated modulations in all related aspects of the series-connected CSCs is compared to summarize the optimal modulation scheme.

3.1 Modulation schemes for current source converters

Series-connected CSCs are composed of multiple identical CSCs. The modulation schemes for series-connected CSCs are identical to those used in a single CSC. They include space vector modulation (SVM), selective harmonics elimination (SHE), and trapezoidal pulse width modulation (TPWM). Their principles will be introduced in the following subsections.

3.1.1 Current source converters

Fig. 3-1 illustrates the series-connected CSC system. The inputs of multiple identical single CSC modules are connected in series to form the DC-link voltage of the system. The outputs of all modules are connected to the grid through a multi-winding transformer. Each CSC requires a three-phase capacitor C_f to assist the commutation of the switching device [28]. In addition, C_f and the leakage inductance L_f of the multi-winding transformer together form an LC filter to improve the

harmonic performance of the load current. The switching frequency f_{sw} of each CSC is about 500 Hz to reduce switching losses and satisfy the stringent thermal requirements of the device [28].

A single CSC consists of six switches (S_1-S_6), and the switches are gate-commutated thyristors (GCTs) with reverse blocking capability. The PWM switching mode of CSC must satisfy a constraint that only two switches are turned on at any time (excluding commutation intervals) in the inverter, one in the upper half of the CSC bridge and the other in the lower half of the CSC bridge [28].

In CSC configurations, the dc-link current I_{dc} can be variable or constant, corresponding to two different ways to achieve power control: 1) Adjusting the modulation index m_a of the converter when I_{dc} is fixed; 2) Adjusting I_{dc} when m_a is fixed. The second way is usually used since it can reduce the conduction losses of the converter [27]. In this chapter, a fixed m_a is set to all modulation schemes so that different modulation schemes can be compared under the same conditions.

All CSCs are identical and share same gate signals. The modulation schemes used in series-connected CSCs are identical as those used in a CSC, mainly including space vector modulation (SVM), selective harmonic elimination (SHE), and trapezoidal pulse width modulation (TPWM). In the following, CSC#1 is taken as an example to illustrate the operation principles of different modulation schemes.

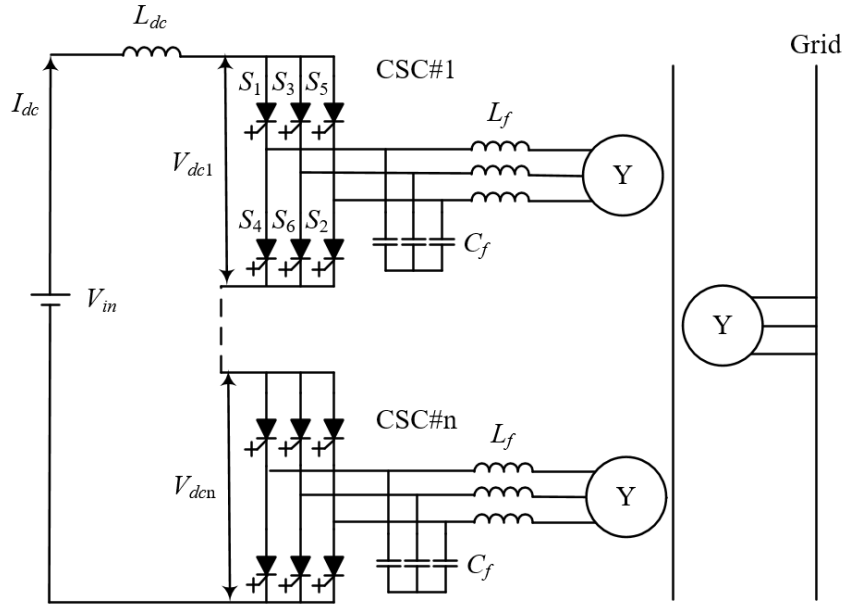

Fig. 3-1 Series-connected CSCs.

3.1.2 Space vector modulation

SVM is an online modulation scheme with superior dynamic performance, the dc current utilization (the ratio of maximum rms fundamental-frequency current $I_{w1,\max}$ to DC-link current I_{dc}) of which is 0.707 [28]. Fig. 3-2 illustrates the space vector diagram for a CSC, where $\vec{I}_{ref}$ represents the current reference vector and rotates at a fixed angular velocity in space, θ is the angle $\vec{I}_{ref}$ turns. Under the switching constraint, the three-phase inverter has a total of 9 switching states listed in Table 3-1, including three zero states and six active states. For example, when S_1 and S_4 in CSC are turned on at the same time, the other four switches are all in the off state and the corresponding space vector is $\vec{I}_0$.

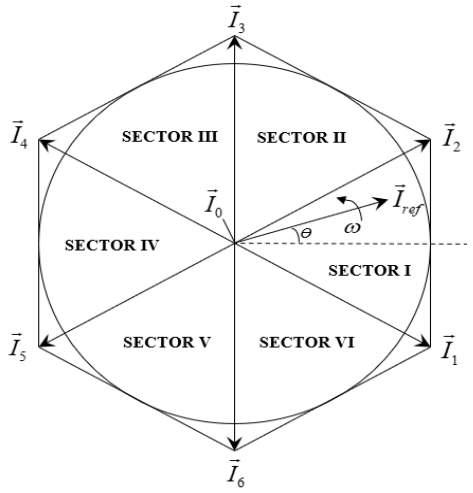

Fig. 3-2 Space vector diagram for CSCs.

For a given length and position, I_{ref} can be synthesized from three nearby fixed vectors, and based on these vectors, the switching state of the inverter can be selected. When I_{ref} crosses different sectors, different switches will be turned on or off. The length of I_{ref} determines the magnitude of the output current, and the speed of I_{ref} corresponds to the output frequency of CSC. The dwell time (T_1, T_2, T_0) of the selected vectors in Sector I is calculated as shown in (3-1) [29-30].

$$\begin{cases} \vec{I}_{ref} T_s = \vec{I}_1 T_1 + \vec{I}_2 T_2 + \vec{I}_0 T_0 \\ T_1 = m_a \sin(\frac{\pi}{3} - \theta) T_s \\ T_2 = m_a \sin(\theta) T_s \\ T_0 = T_s - T_1 - T_2 \end{cases} \tag{3-1}$$

where m_a is the modulation index, θ is the angle of I_{ref}, T_s is the sampling period. I_1 and I_2 are the active space vectors in Sector I, active space vectors will change in other sectors.

Switching sequence design needs to follow two requirements for the minimization of switching frequencies: 1) Only two switches are involved (one being turned on and one being turned off) when switching between two switching states; and 2) Requiring the minimum number of switching when I_{ref} traverses different sectors.

Table 3-1 Switching States and Space Vectors

Type	Space Vector	On-state Switches
Zero states	$\vec{I}_0$	S_1&S_4
		S_2&S_5
		S_3&S_6
Active States	$\vec{I}_1$	S_6&S_1
	$\vec{I}_2$	S_1&S_2
	$\vec{I}_3$	S_2&S_3
	$\vec{I}_4$	S_3&S_4
	$\vec{I}_5$	S_4&S_5
	$\vec{I}_6$	S_5&S_6

These sequences consist of different arrangements of space vectors. In each T_s (or 2 T_s), dwell times T_1, T_2, T_0 are arranged in a specific order. In this way, the switch state of the converter can be obtained at any time. Based on the above principles, there are six mostly discussed switching sequences in the literature [29-36].

1) SQ1

Fig. 3-3 (a) shows the arrangement of SQ1 in each sampling period T_s. The sampling frequency f_{sp} is 1080Hz, and there are 3 vectors in each T_s, which occupy dwell time T_1, T_2 and $T_{0,}$ respectively. The device switching frequency f_{sw} is 540 Hz, corresponding to nine pulses of i_w in Fig. 3-3(b).

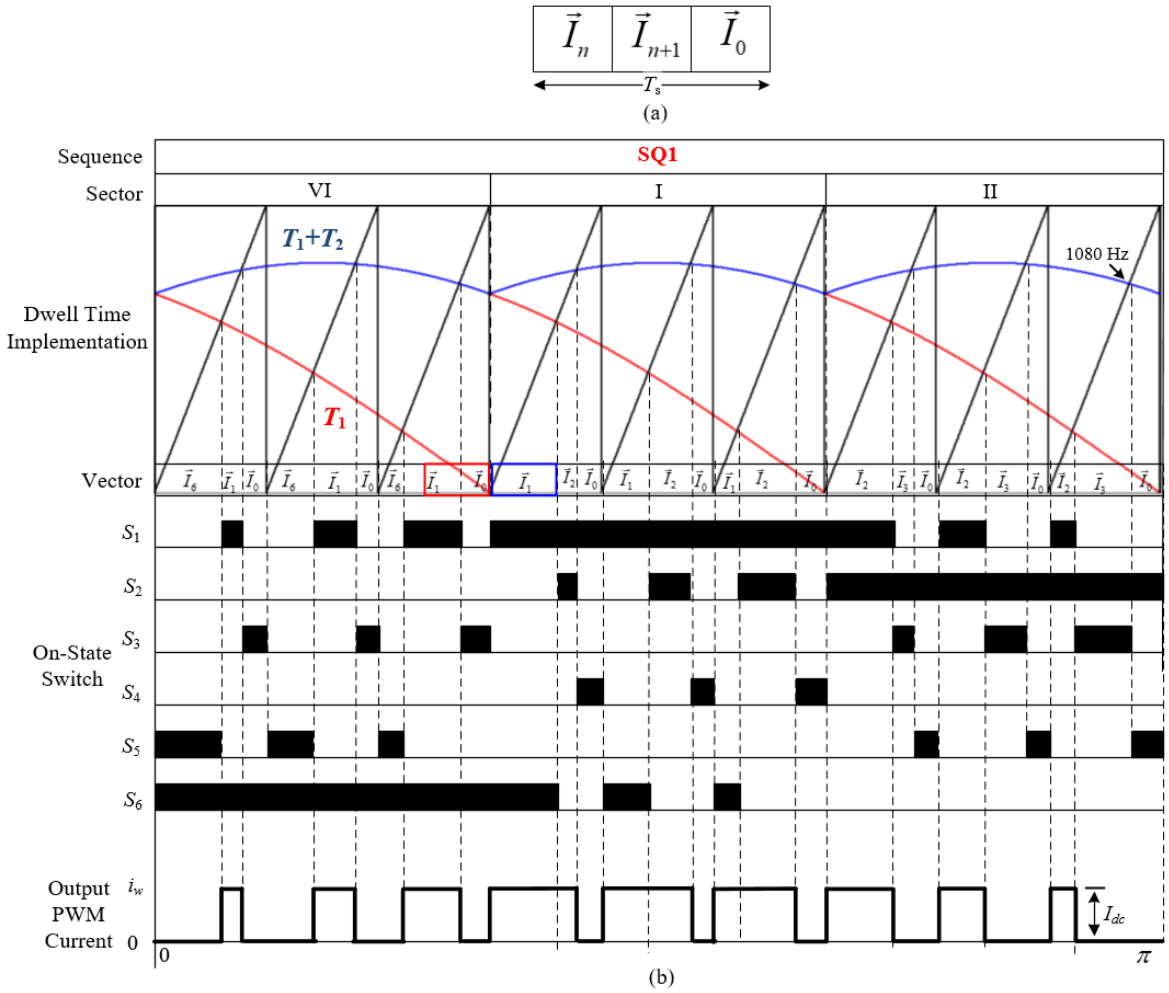

Fig. 3-3 SVM switching sequence SQ1.

2) SQ2

Fig. 3-4 (a) shows the arrangement of SQ2 in each sampling period T_s. The sampling frequency f_{sp} is 1080Hz. Compared to SQ1, the zero state is divided into two segments in each T_s, each occupying half of the dwell time T_0. The device switching frequency f_{sw} is 540 Hz, corresponding to nine pulses of i_w in Fig. 3-4 (b).

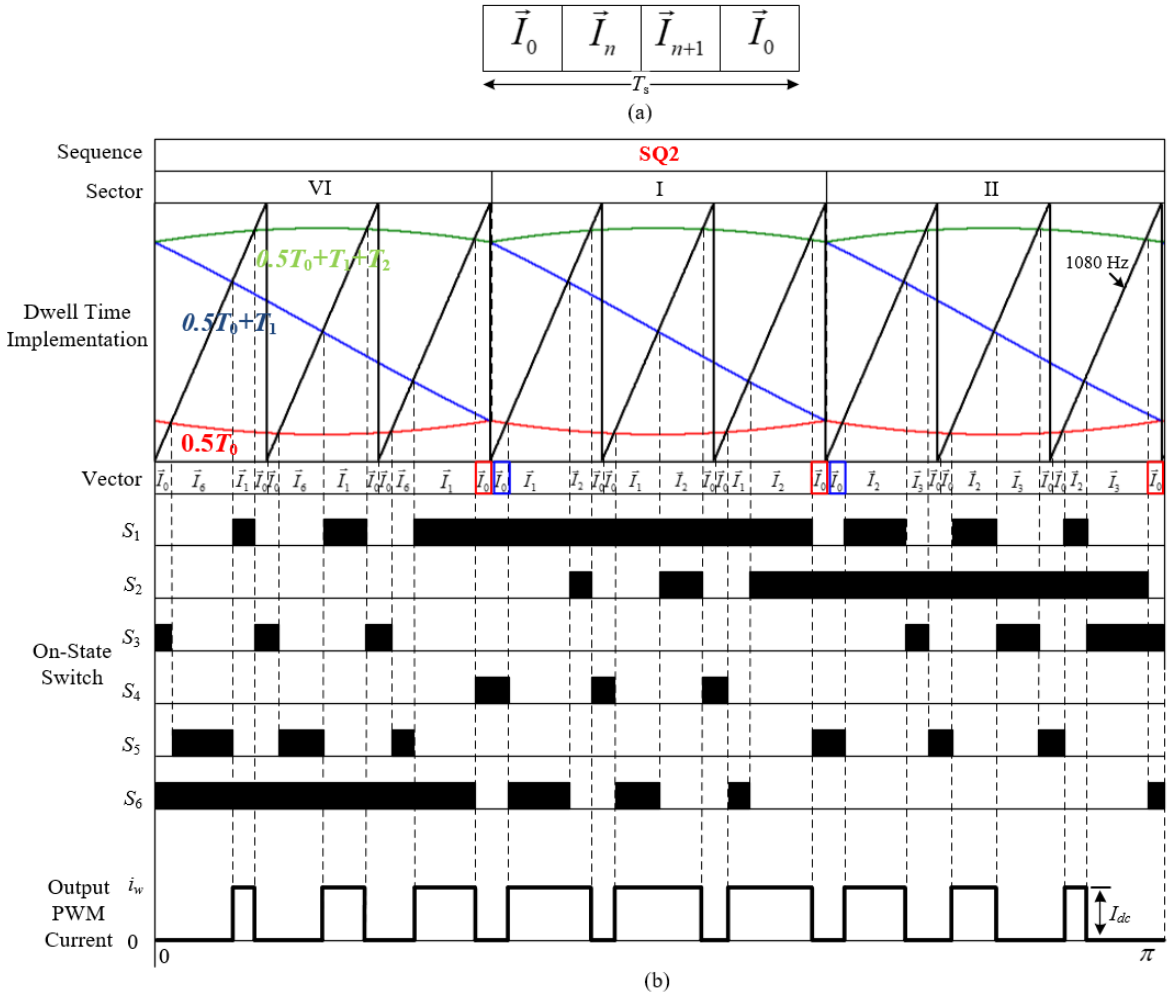

Fig. 3-4 SVM switching sequence SQ2.

3) SQ3

Fig. 3-5 (a) shows the arrangement of SQ3 in each sampling period T_s. The sampling frequency f_{sp} is 1080Hz. Compared to SQ1, the arrangement order of the vectors is changed. Due to the change of arrangement order, the last switching state of each sector is equal to the first switching state of the next sector, which saves one-ninth of the number of switching. The device switching frequency f_{sw} is then reduced to 480 Hz, corresponding to eight pulses of i_w in Fig. 3-5 (b).

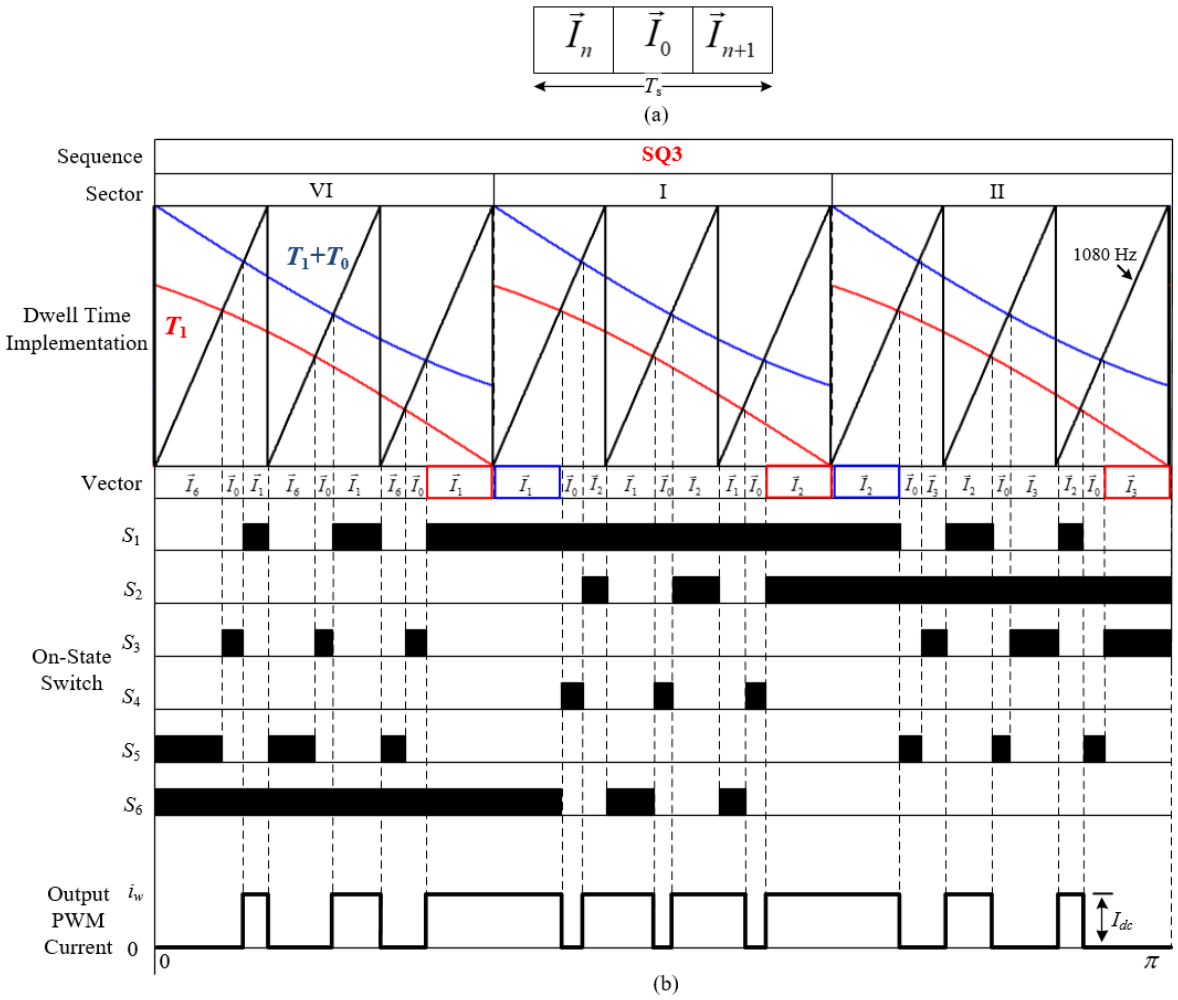

Fig. 3-5 SVM switching sequence SQ3.

4) SQ4

Fig. 3-6 (a) shows the arrangement of SQ4. The sampling frequency f_{sp} is 1080Hz. SQ4 presents the same pattern every two sampling periods. In addition, there are two different zero states in one sampling period, each occupying half of the dwell time T_0. The device switching frequency f_{sw} is 540 Hz, corresponding to nine pulses of i_w in Fig. 3-6 (b).

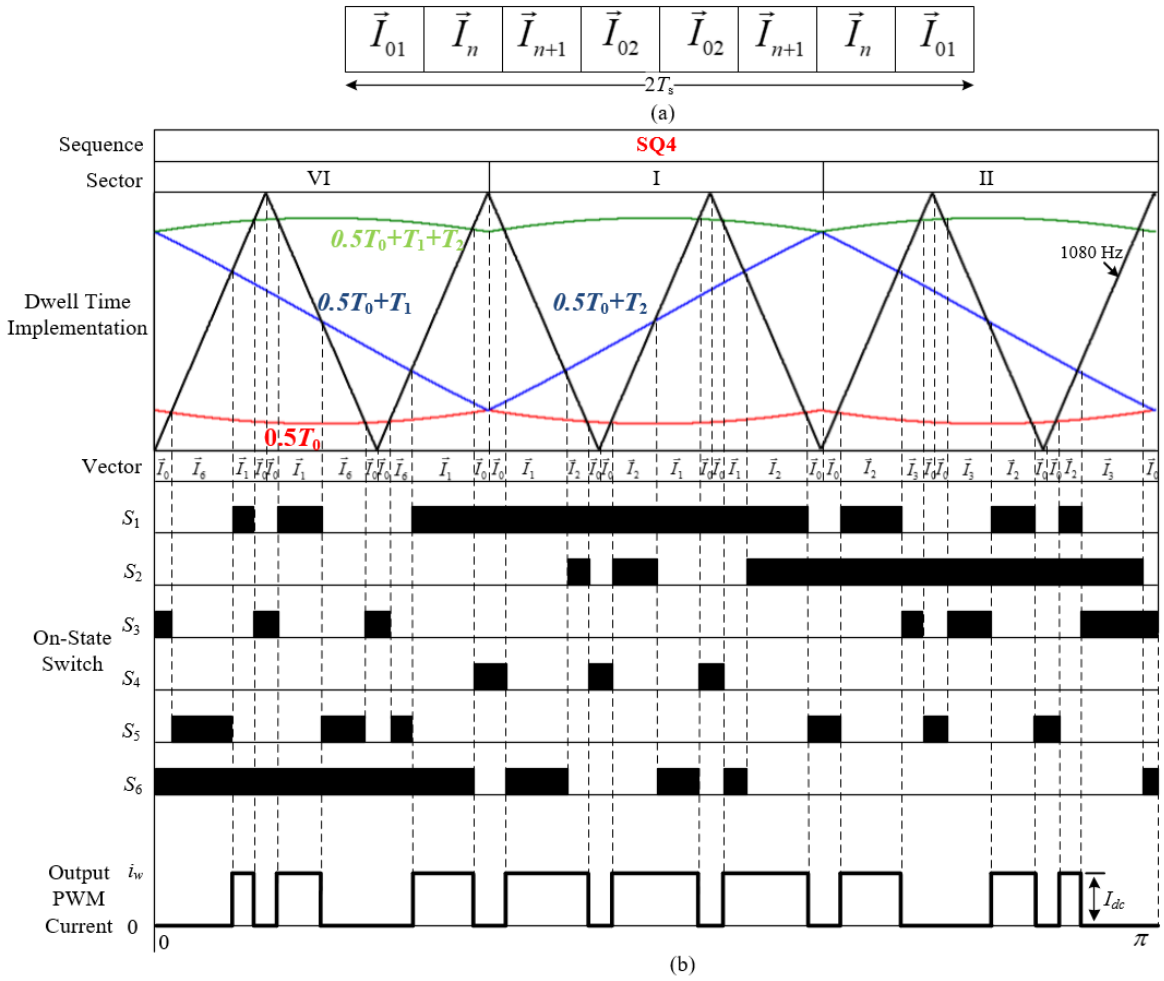

Fig. 3-6 SVM switching sequence SQ4.

5) SQ5

Fig. 3-7 (a) shows the arrangement of SQ4. The sampling frequency f_{sp} is 1440Hz. SQ5 presents the same pattern every two sampling periods. In addition, similar to SQ3, the last switching state of each sector is equal to the first switching state of the next sector, which saves one-ninth of the number of switching. The device switching frequency f_{sw} is reduced to 480 Hz, corresponding to eight pulses of i_w in Fig. 3-7 (b).

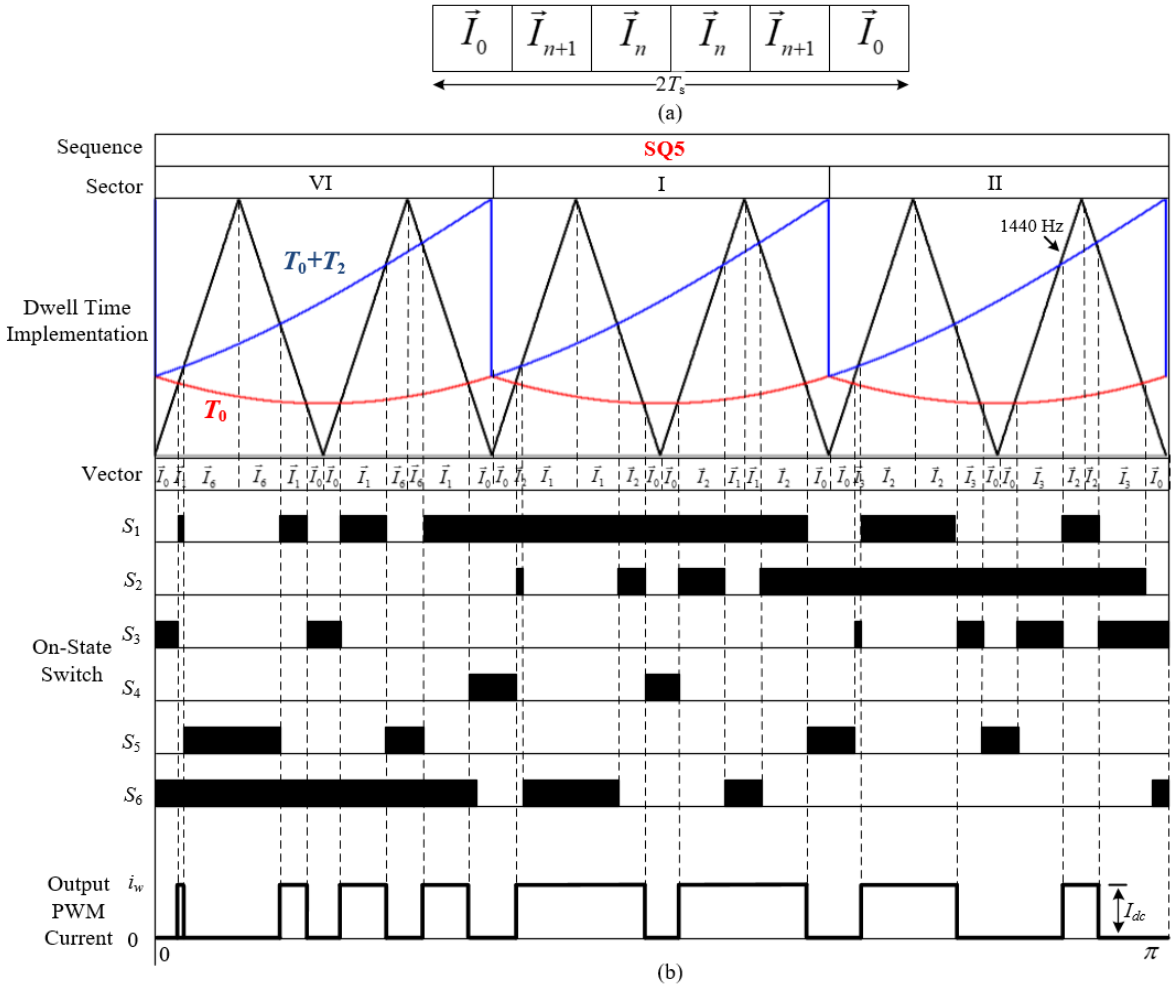

Fig. 3-7 SVM switching sequence SQ5.

1) SQ6

Fig. 3-8 (a) shows the arrangement of SQ6. The sampling frequency f_{sp} is 1440Hz. SQ6 presents the same pattern every two sampling periods. The device switching frequency f_{sw} is 540 Hz, corresponding to nine pulses of i_w in Fig. 3-8 (b).

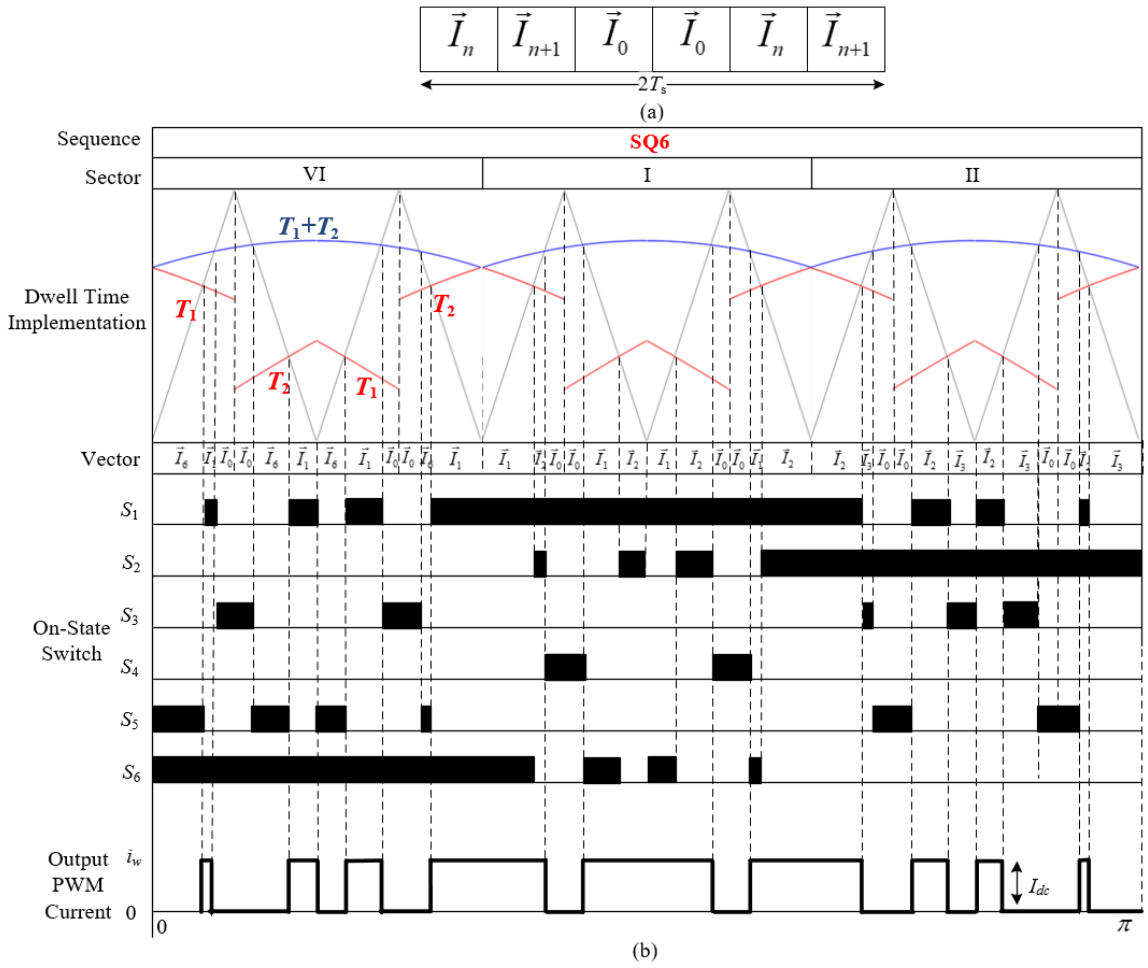

Fig. 3-8 SVM switching sequence SQ6.

3.1.3 Selective harmonic elimination

SHE is an offline modulation scheme that can eliminate a couple of unwanted low-order harmonics in the inverter PWM current i_w [37-39]. It's implemented by pre-calculating the switching angles and then importing them into the digital controller. Fig. 3-9 shows a 9-pulse SHE waveform (f_{sw} = 540 Hz) that satisfies the switching constraint for the CSI. In the first half cycle (0- π), there are nine pulses (N_p = 540/60 = 9) with 9 switching angles (different number of switching angles under different f_{sw}) in the first π/2 period. However, only 4 out of 9 angles (θ_1 - θ_4) are independent. Given these 4 angles, all other switching angles can be calculated. These 4 switching angles provide 4 degrees of freedom and can be used to eliminate 4 different harmonics in i_w. Different sets of harmonics can be eliminated by the combination of different switching angles, and the values of these angles can be

obtained by solving different equations. By using the Newton–Raphson Iteration Algorithm, the specific values of the switching angles are calculated. When using different combinations of switching angles, the dc current utilization of SHE will float within 0.73-0.78.

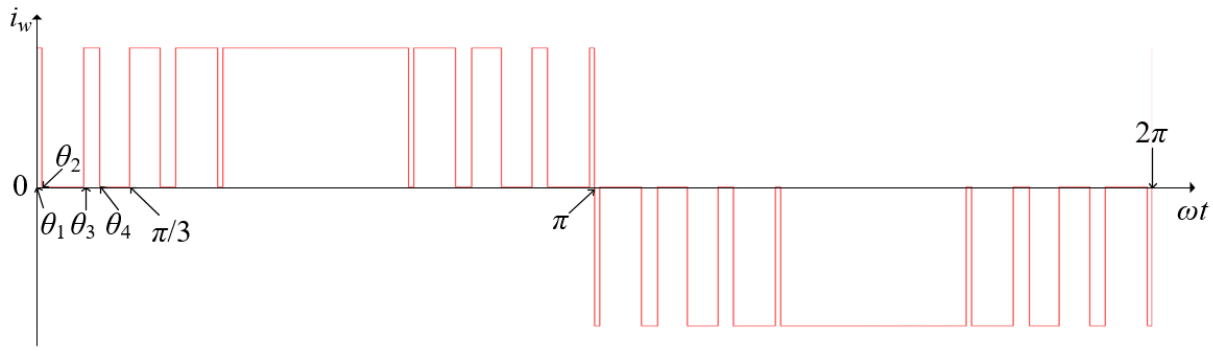

Fig. 3-9 9-pulse selective harmonic elimination (SHE) scheme.

3.1.4 Trapezoidal pulse width modulation

Fig. 3-10 shows the principle of TPWM when the switching frequency f_{sw} = 540 Hz. The signals for switches are generated by comparing the modulating wave with the carrier wave [40]. In each cycle: 1) the modulating wave is a trapezoidal wave, which is at low level in half a cycle, and at high level in the middle one-third of the other half cycle; 2) the carrier wave equals to zero when the modulating wave reaches high level or low level; and 3) the carrier wave is a triangle wave the rest of time, and the frequency of which is related to f_{sw}. The signals of other switches can be obtained by shifting the signal for S_1. It is worth mentioning that there is no zero state in TPWM, which means the bypass operation cannot be performed. And because of this, its dc current utilization is higher than SVM, which is 0.74. The active states are the same as the SVM in Table 3-1.

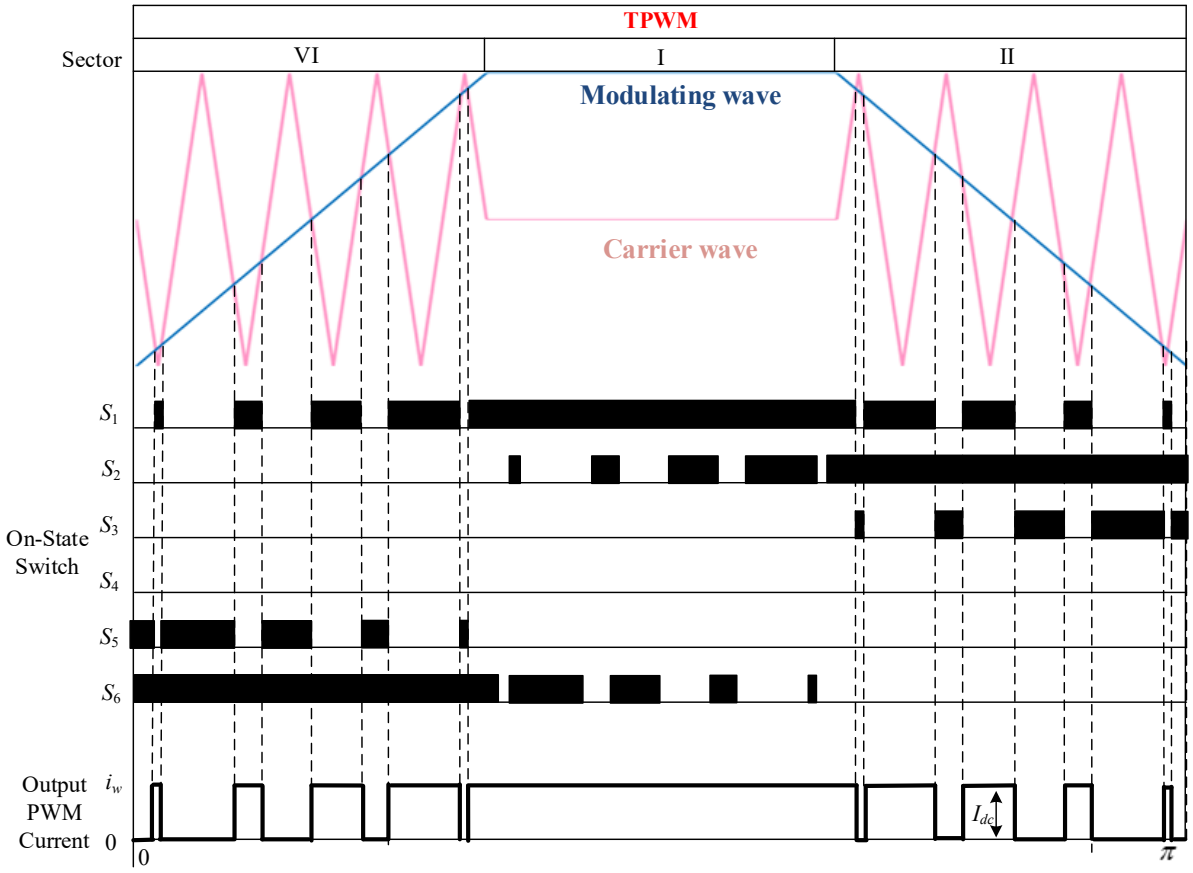

Fig.3-10 Trapezoidal pulse width modulation.

3.1.5 Criteria of optimal modulation scheme investigation

Different modulation schemes (TPWM, SHE, and all SVM switching sequences) have different performance. The performance of modulation schemes for a CSC has been well studied in the literature [28-40]. As shown in Table 3-2, a thorough comparison between different modulation schemes is made in terms of DC current utilization, dynamic performance, digital implementation, harmonic performance, and DC current bypass operation [28].

However, the performance of modulation schemes for the grid-side series-connected CSCs of the proposed wind energy conversion system has not been conducted. The DC-link inductor used in the series-connected CSCs is n (the number of CSC used) times as high as that of a CSC. Therefore, apart from those items shown in Table 3-2, the DC-link inductor sizing should be considered when investigating the optimal modulation scheme for the series-connected CSCs.

To sum up, the items to be investigated in this chapter include: 1) sizing of the DC-link inductor, 2) harmonic performance, 3) DC current utilization, 4) dynamic performance, 5) digital implementation, and 6) DC current bypass operation. On this basis, the optimal modulation will be selected.

Table 3-2 Conventional Performances of Different Modulation Schemes [28]

	SVM	TPWM	SHE
DC current utilization	0.707	0.74	0.73-0.78
Dynamic performance	High	Medium	Low
Digital implementation	Real time	Real time or look up table	Look-up table
Harmonic performance	Adequate	Good	Best
DC current bypass operation	Yes	No	Optional

3.2 DC-link inductor investigation

In CSC-based systems, the DC-link inductor (L_{dc}) is used to make dc-link current I_{dc} smooth and continuous. This inductor is bulky and costly, according to previous investigations, that it is approximately 0.6 pu at a switching frequency of around 500 Hz [28]. In series-connected CSCs, the demand for this inductance is multiplied since multiple CSCs share the same dc-link.

This section first analyzes all the factors that affect the dc-link inductance followed by the study of the relationship between the dc-link inductance and the modulation schemes. Then the required dc-link inductance under all the modulation schemes (including the six switching sequences of SVM) is calculated and compared. The modulation scheme with the least L_{dc} is obtained.

3.2.1 DC-link inductance calculation

Fig. 3-11 illustrates the simplified circuit of the series-connected CSCs, where V_{in} and v_{dc} are the voltages before and after L_{dc}. In a series-connected CSC system, v_{dc} is equal to the sum of the input voltages of each individual CSC (v_{dc1}-v_{dcn}), as shown in (3-2). $v_{dc1} = v_{dcn}$ is due to identical gating signals applied to each CSC.

$$v_{dc1} = v_{dc2} = \cdots = v_{dcn} = \frac{v_{dc}}{n} \tag{3-2}$$

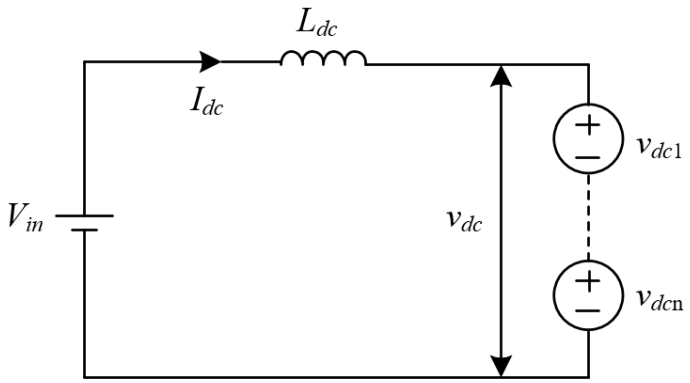

Fig. 3-11 Simplified circuit of series-connected CSCs.

The equation for the DC-link inductor calculation is expressed as shown in (3-3). V_{in} comes from generator-side and can be seen as a constant voltage, v_{dc} is the sum of the input voltages of all series-connected converters, ΔI_{dc} is the peak to peak DC current ripple, 12% of I_{dc}, for example, and Δt is the dwell time.

$$L_{dc} = \frac{|V_{in} - v_{dc}|\Delta t}{\Delta I_{dc}} = \frac{|V_{in} - nv_{dc1}|\Delta t}{\Delta I_{dc}} \tag{3-3}$$

As illustrated in Fig. 3-11, since the system is grid-connected, the input voltage of each CSC (v_{dc1} to v_{dcn}) under all switching states is clamped by the grid voltage. The relationship between different switching states and the grid voltage is listed in Table 3-3. For example, when S1 and S6 are on (switching state [61]), the input voltage (v_{dc1}) of the CSC #1 is equal to the terminal voltage (v_{ab}) of the CSC and clamped by the grid voltage. The terminal voltages of the CSC are given in (3-4), where V_g is the rms grid phase voltage, and θ is the angle of current reference which is related to the grid, LC filter, and power factor. Fig. 3-13 shows the waveform of the input voltage of the CSC #1 over 2π.

Table 3-3 Switching States and the Grid Voltage v_{dc1}

Switching states	[14]	[25]	[36]	[61]	[12]	[23]	[34]	[45]	[56]
v_{dc1}	0			v_{ab}	v_{ac}	v_{bc}	v_{ba}	v_{ca}	v_{cb}

$$\begin{cases} v_{ab} = \sqrt{3}V_g \cos(\theta + \frac{\pi}{6}) \\ v_{ac} = \sqrt{3}V_g \cos(\theta - \frac{\pi}{6}) \\ v_{bc} = \sqrt{3}V_g \cos(\theta - \frac{\pi}{2}) \\ v_{ba} = \sqrt{3}V_g \cos(\theta - \frac{5\pi}{6}) \\ v_{ca} = \sqrt{3}V_g \cos(\theta + \frac{5\pi}{6}) \\ v_{cb} = \sqrt{3}V_g \cos(\theta + \frac{\pi}{2}) \end{cases} \tag{3-4}$$

Shown in (3-3), under the condition of a constant dc current ripple, the variables that affect L_{dc} are v_{dc} and Δt. They are related to the chosen modulation schemes. When using different modulation schemes, v_{dc} and Δt are different and the value of L_{dc} required is different.

Shown in Fig. 3-12, v_{dc1} and Δt repeat every sector (one-sixth of the fundamental period), while during each sector, different v_{dc1} with different magnitudes and dwell times exist and different minimum dc inductances will be generated. Among all these values, the maximum one should be selected to ensure the current ripple is equal or below the required. In the following, Sector I is taken as an example to illustrate the DC-link inductor calculation.

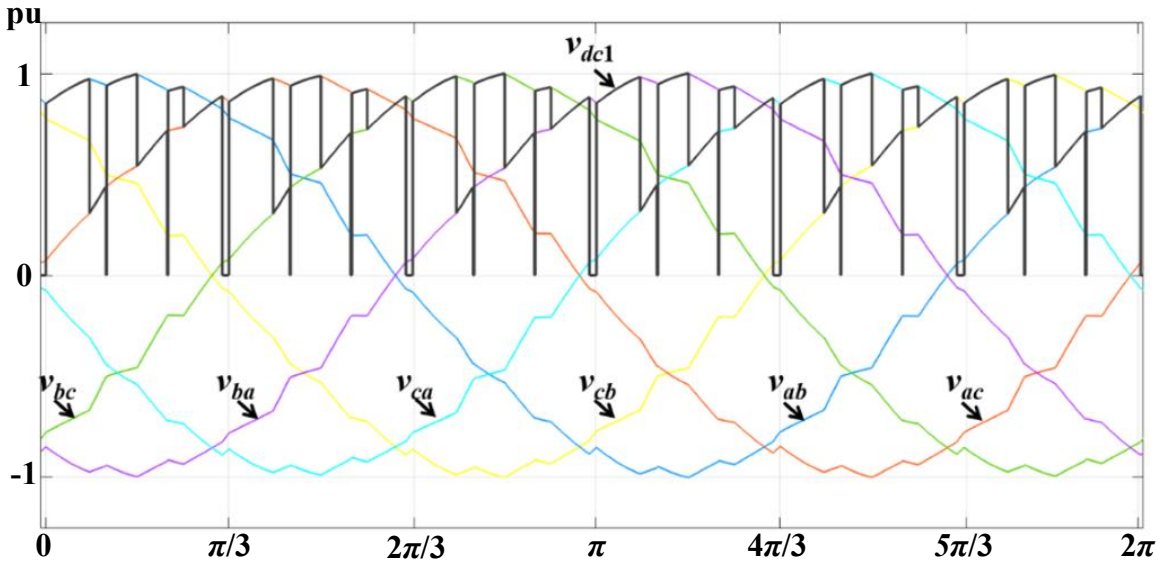

Fig. 3-12. Input voltage v_{dc1} of a single CSC (taking SQ1 as an example).

3.2.2 DC-link inductance under different modulation schemes

Substituting (3-2) and (3-4) into (3-3) gives the required dc inductance as shown in (3-5), where *m* represents the m-th switching state that occurs in Sector 1. Noted that the number m is not fixed and is determined by the adopted modulation scheme. For example, in the case of SQ1, there are three sampling periods in each sector, each sampling period has three switch states, and then m = 3*3 = 9. Similarly, m=12 for SQ2 since each sampling period has four switching states.

$$\begin{cases} L_{dcm} = \dfrac{\left| V_{in} - \dfrac{1}{\Delta t_m}\displaystyle\int_t^{t+\Delta t_m} \left\{\sqrt{3}V_g \cos\theta_m\right\} d\theta_m \right| \Delta t_m}{12\% I_{dc}} \\ L_{dc} = \max\left\{L_{dc1}, L_{dc2}, \ldots, L_{dcm}\right\} \end{cases} \tag{3-5}$$

Fig. 3-13 shows the waveforms of v_{dc} and V_{in} when using SQ2. In the figure, L_{dc} can be regarded as the area sandwiched between the v_{dc} and V_{in} waveforms, divided into 12 parts, the largest part of which is the minimum L_{dc} required. The detailed calculation formula of the dc-link inductance for SQ2 is derived as shown in (3-6).

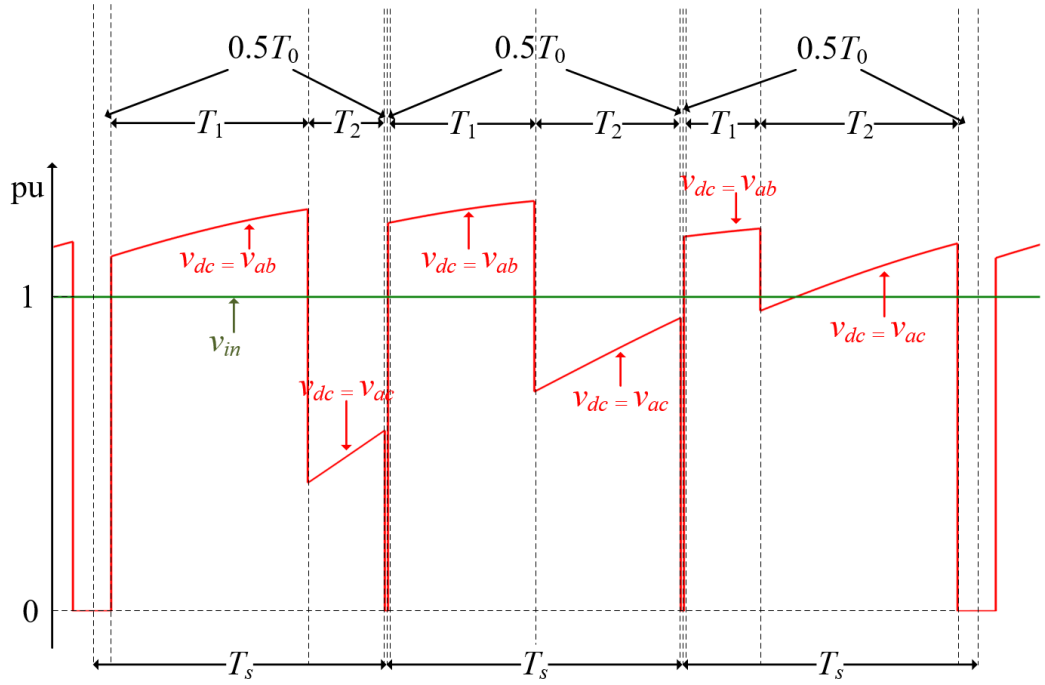

Fig. 3-13 Waveforms of V_{dc} and V_{in} in SQ2.

$$
\begin{cases}
L_{dc1} = \dfrac{|V_{in} - 0|\dfrac{T_0}{2}}{12\% I_{dc}} \\
L_{dc2} = \dfrac{\left| V_{in} - \dfrac{1}{T_1}\int_{T_0/2}^{T_1+T_0/2} \left\{ \sqrt{3} V_g \cos(\theta + \dfrac{\pi}{6}) \right\} d\theta \right| T_1}{12\% I_{dc}} \\
L_{dc3} = \dfrac{\left| V_{in} - \dfrac{1}{T_2}\int_{T_1+T_0/2}^{T_2+T_1+T_0/2} \left\{ \sqrt{3} V_g \cos(\theta - \dfrac{\pi}{6}) \right\} d\theta \right| T_2}{12\% I_{dc}} \\
\vdots \\
L_{dc12} = \dfrac{|V_{in} - 0|\dfrac{T_0}{2}}{12\% I_{dc}} \\
L_{dc} = \max\{L_{dc1}, L_{dc2}, \ldots, L_{dc12}\}
\end{cases}
\tag{3-6}
$$

The above method applies to all modulation schemes and sequences, thus not repeated here. At a switching frequency of around 500Hz, the minimum L_{dc} of all modulation schemes is calculated and shown in Table 3-4, where n represents the number of CSCs connected in series. It is concluded that in the performance of dc-link inductance, SHE is the optimal modulation scheme.

Table 3-4 L_{dc} under Different Modulation Schemes

Modulation Scheme	L_{dc} (pu)
SVM(SQ1)	$0.6n^2$
SVM(SQ2)	$0.56n^2$
SVM(SQ3)	$0.95n^2$
SVM(SQ4)	$0.74n^2$
SVM(SQ5)	$1.03n^2$
SVM(SQ6)	$0.77n^2$
SHE	$0.54n^2$
TPWM	$0.77n^2$

3.2.3 Simulated verification

In the simulation, two CSCs are connected in series to verify the analysis and calculation above. To investigate the performance of different modulation schemes in the sizing of the DC inductor, a same L_{dc} is set purposely for all investigated modulations, and the corresponding DC current ripples (ΔI_{dc}) are measured and compared. The simulation parameters are shown in Table 3-5.

Fig. 3-14 shows the waveforms of I_{dc} under all modulation schemes and sequences, respectively. As shown in Fig. 3-14, under a same DC inductor, SHE is with the smallest DC current ripple. In turn, given a DC current ripple, the use of the SHE modulation requires the smallest DC inductor, which verifies the previous analysis. SHE is the optimal modulation scheme in terms of the DC inductor sizing.

Table 3-5 Simulation Parameters

Nominal Power	2*1MW
Grid Voltage	2*4160V
Fundamental Frequency	60Hz
Switching Frequency	540Hz (480Hz in SQ3 and SQ5)
Modulation Index	1
DC-Link Voltage	2*5000V
DC-Link Current	200A
DC-Link Inductance	2*27.3mH

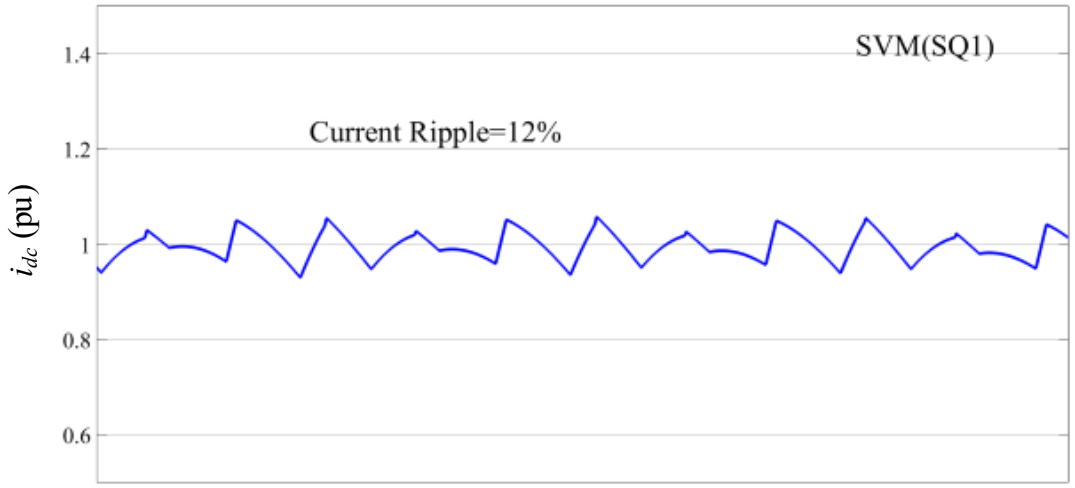
SVM(SQ1)
Current Ripple=12%
i_{dc} (pu)
1.4
1.2
1
0.8
0.6

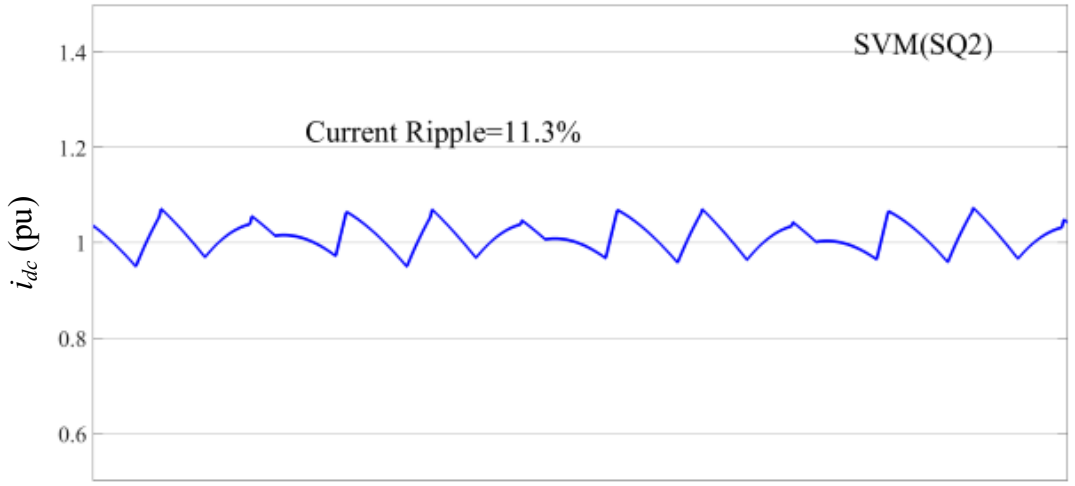
SVM(SQ2)
Current Ripple=11.3%
i_{dc} (pu)
1.4
1.2
1
0.8
0.6

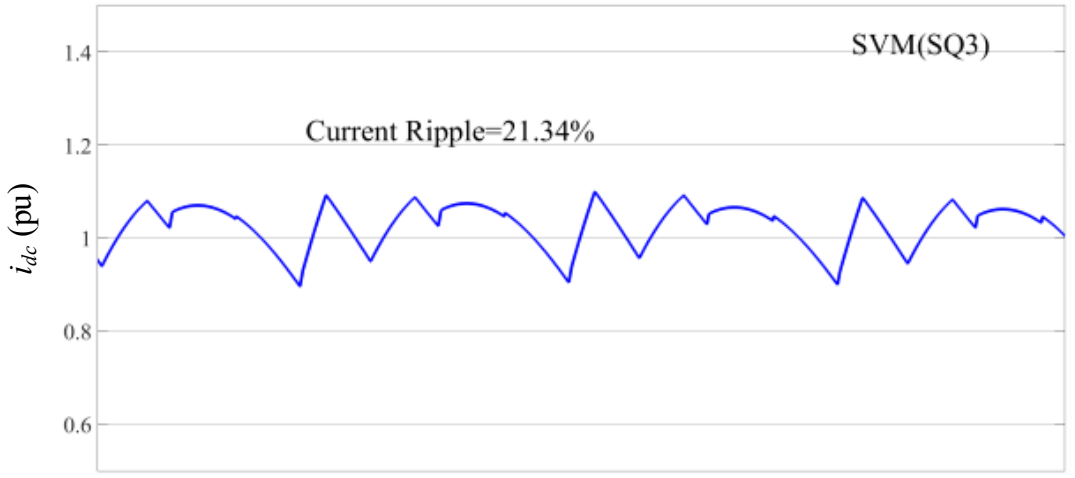
SVM(SQ3)
Current Ripple=21.34%
i_{dc} (pu)
1.4
1.2
1
0.8
0.6

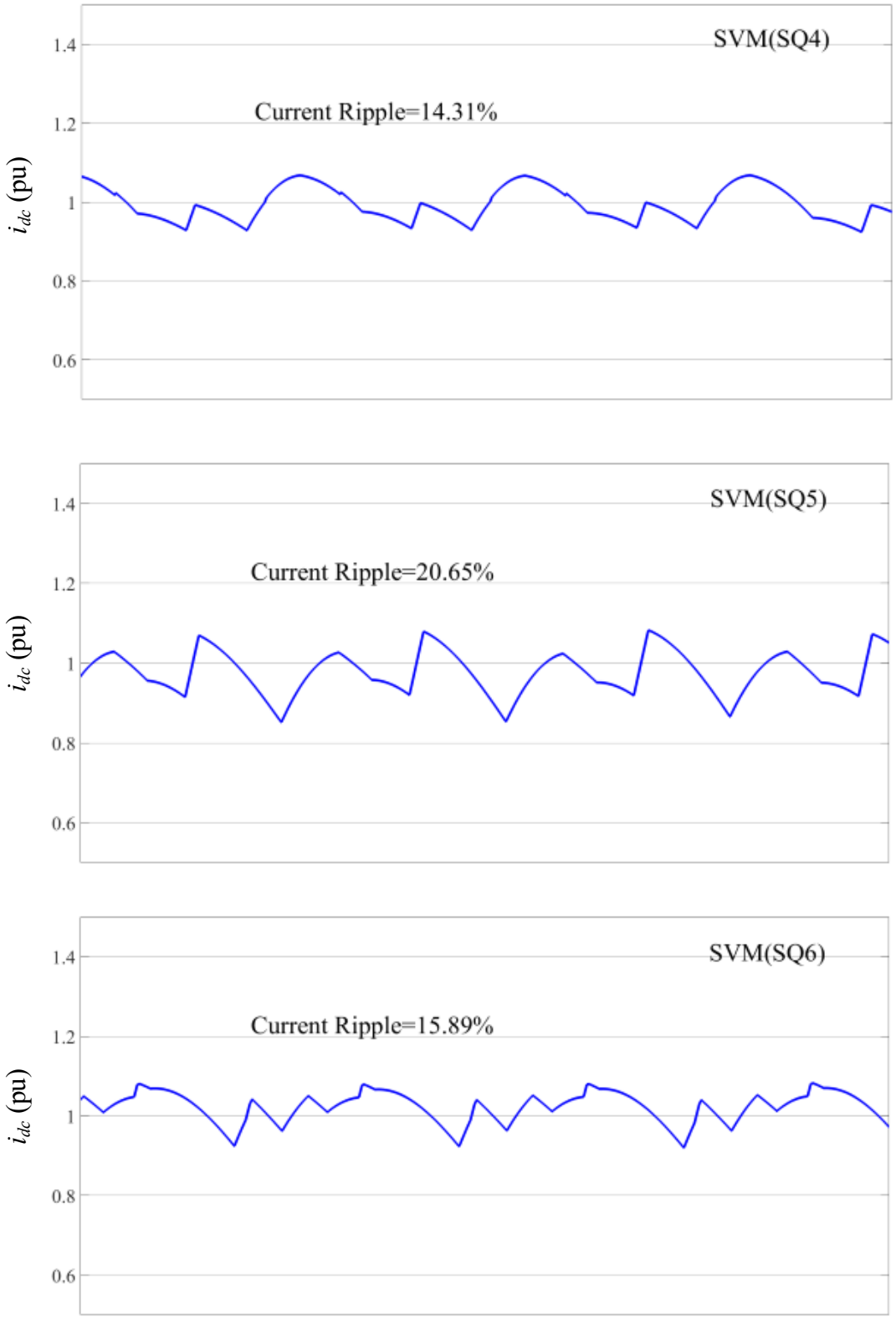
SVM(SQ4)
Current Ripple=14.31%
i_{dc} (pu)
1.4
1.2
1
0.8
0.6
SVM(SQ5)
Current Ripple=20.65%
i_{dc} (pu)
1.4
1.2
1
0.8
0.6
SVM(SQ6)
Current Ripple=15.89%
i_{dc} (pu)
1.4
1.2
1
0.8
0.6

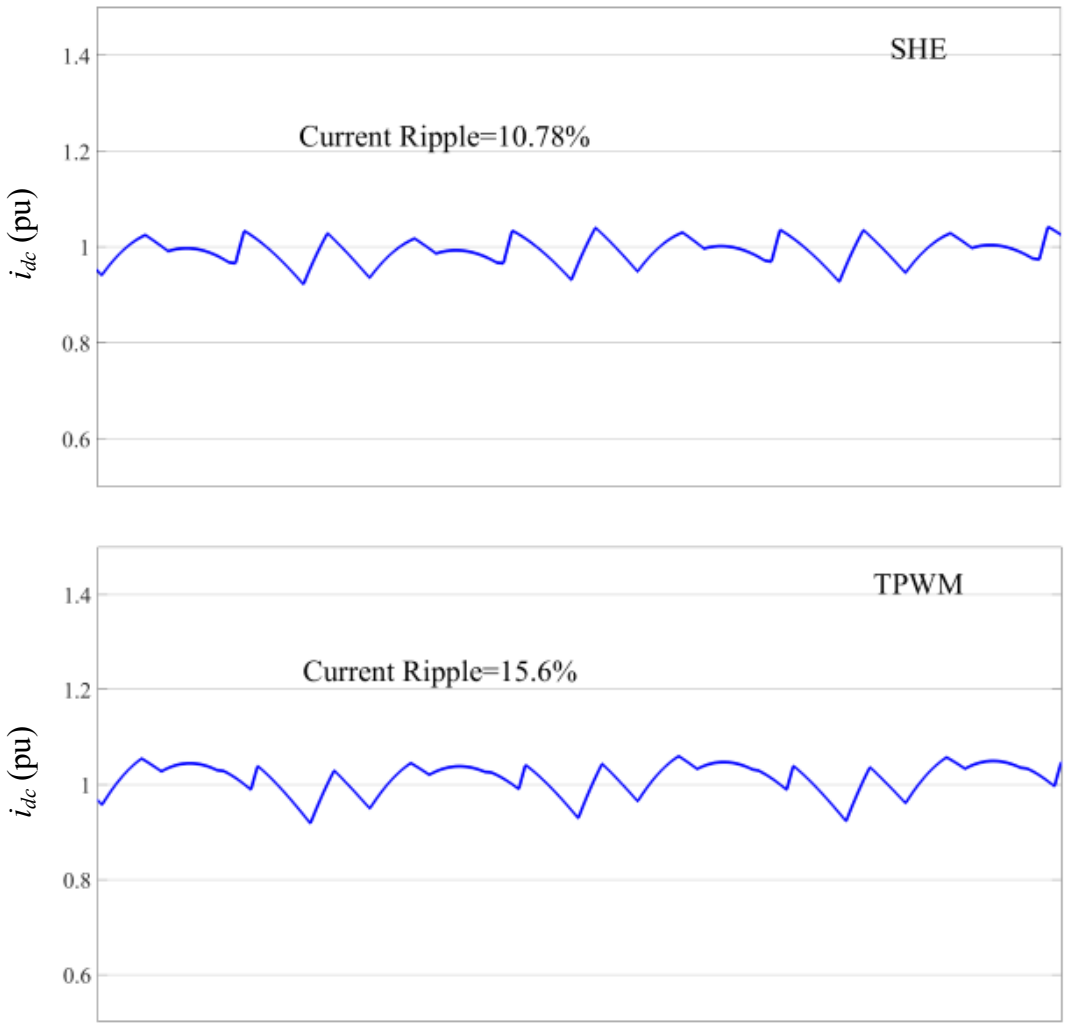

Fig. 3-14 Waveforms of I_{dc}(pu) in different modulation schemes and sequences.

3.3 Harmonic performance investigation

The harmonic performance of the adopted modulation scheme is a very important aspect. The PWM current i_w generated by CSC becomes sinusoidal current i_s through the LC filter and is finally connected to the grid. Because grid codes have strict requirements on the harmonic content of i_s, the harmonic content of i_w determines the size of the LC filter. In other words, a modulation scheme with good harmonic performance requires a small LC filter, which will reduce the cost. Since i_w is a half-wave symmetrical three-phase current, there is no even order harmonics and 3rd, 9th, 15th, 21st …harmonics.

It is worth noting that the low-order harmonics (5th and 7th) are more critical because they have a greater impact on the size of the LC filter. The design of the LC filter will be introduced in the next section. This section analyzes the harmonic performance of all modulation schemes (including all SVM switching sequences) with the help of the MATLAB/Simulink simulation.

The simulation parameters are the same as those listed in Table 3-5 in 3.2.3. Using the Fourier transform in Simulink, the harmonics of i_w with different modulation schemes are obtained, respectively, as shown in Fig. 3-15:

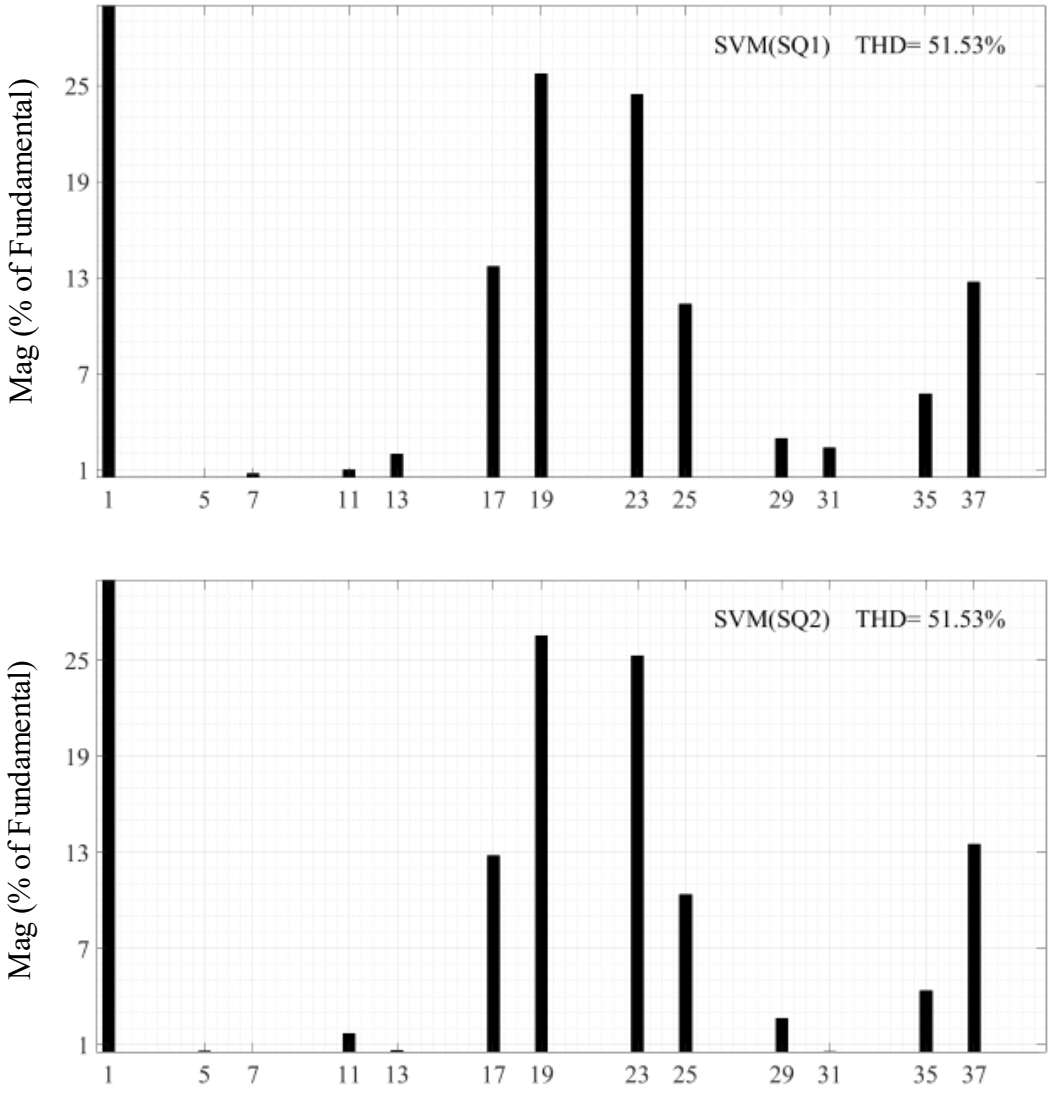

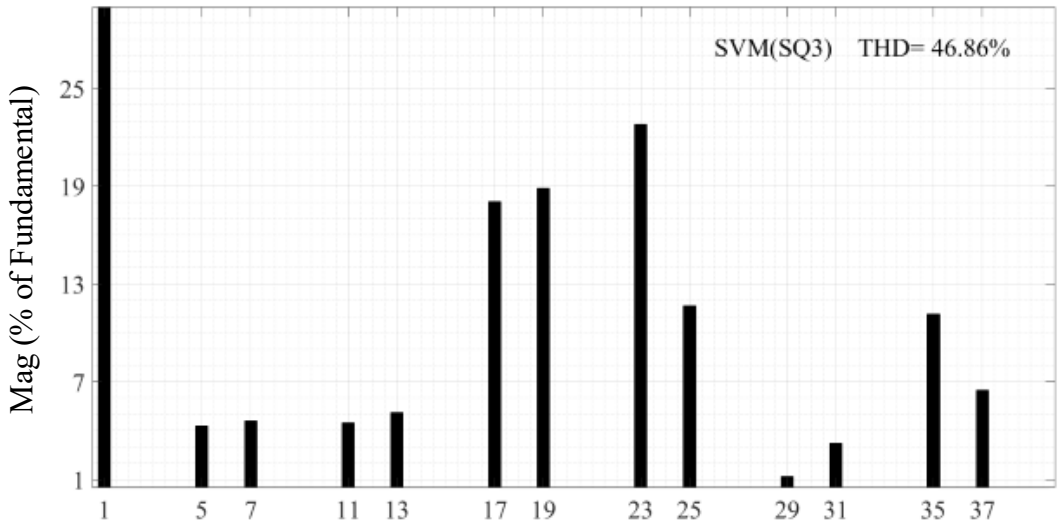
SVM(SQ3) THD= 46.86%
Mag (% of Fundamental)
25
19
13
7
1
1 5 7 11 13 17 19 23 25 29 31 35 37

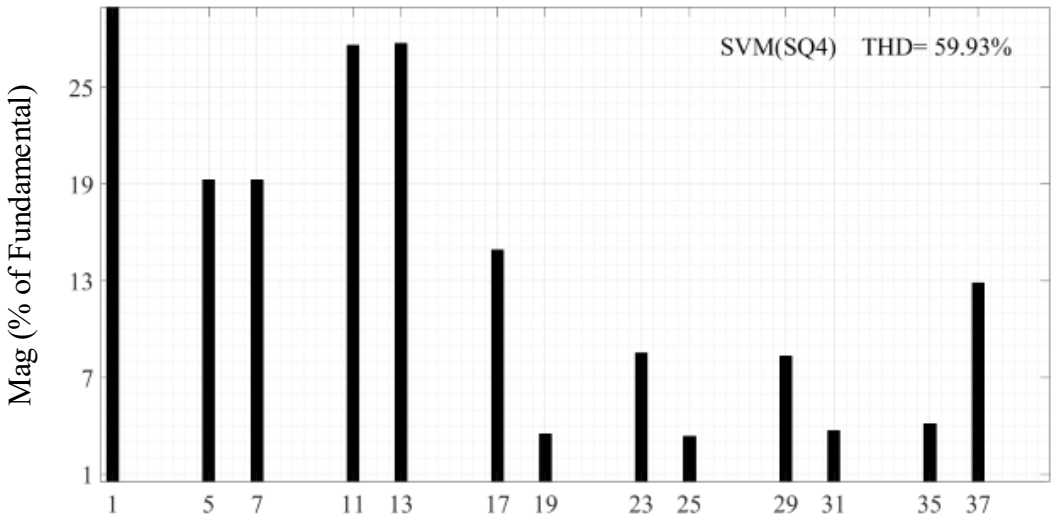
SVM(SQ4) THD= 59.93%
Mag (% of Fundamental)
25
19
13
7
1
1 5 7 11 13 17 19 23 25 29 31 35 37

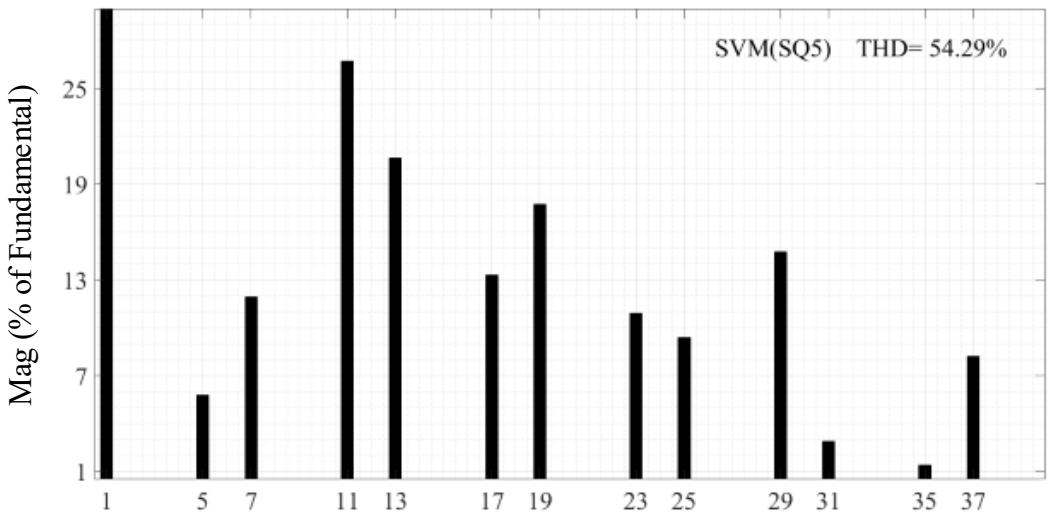
SVM(SQ5) THD= 54.29%
Mag (% of Fundamental)
25
19
13
7
1
1 5 7 11 13 17 19 23 25 29 31 35 37

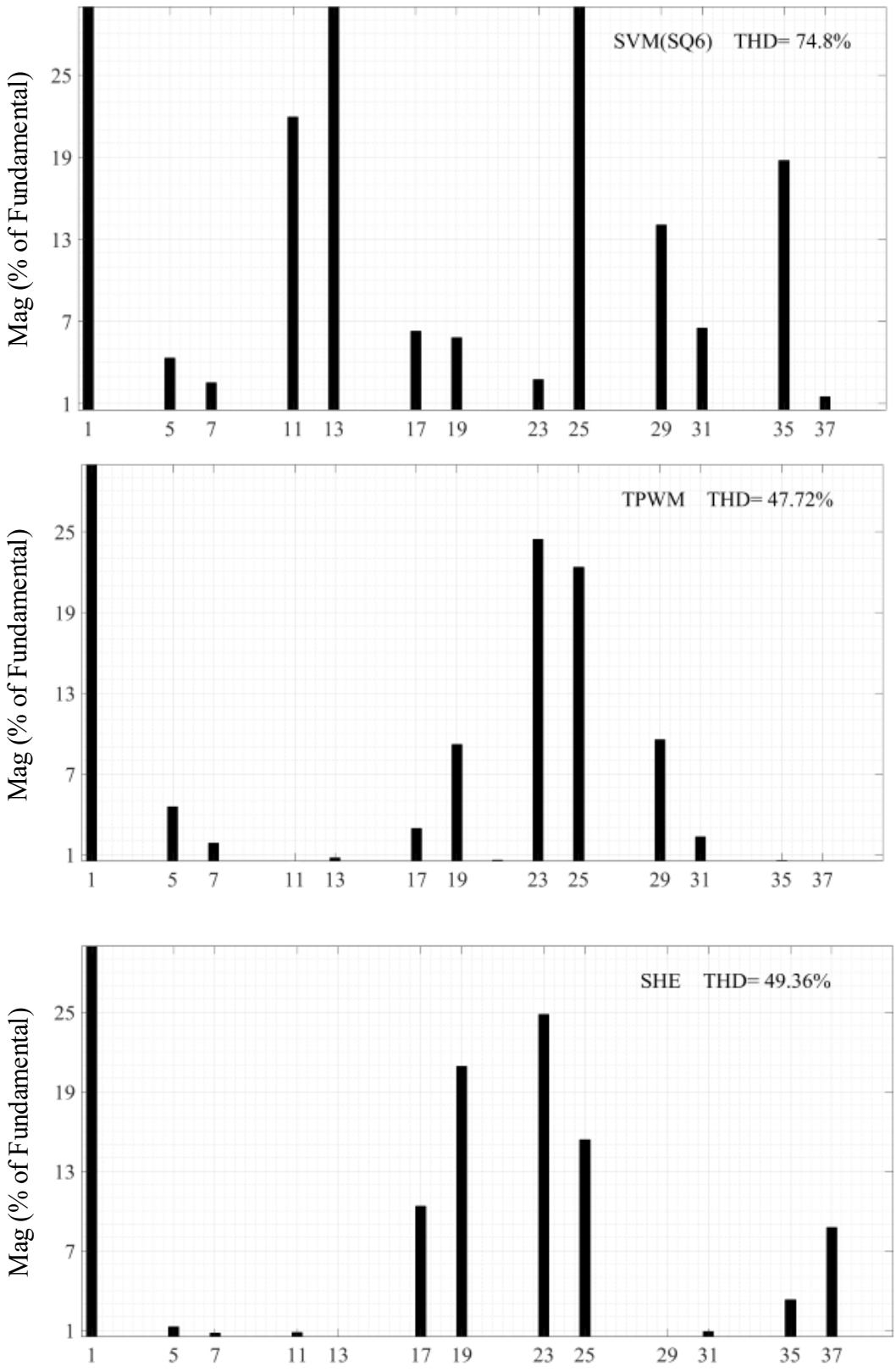

Fig. 3-15 Harmonic performances of all modulation schemes and sequences.

Table 3-6 shows harmonics below the 40th order under all modulation schemes and sequences. It turns out that different modulation schemes have different harmonic performance, and the SQ1, SQ2 and SHE perform better in low-order harmonics performance.

Table 3-6 Harmonics below the 40th Order

Harmonics of I_w	TPWM	SHE	SQ1	SQ2	SQ3	SQ4	SQ5	SQ6
5th (%)	4.57	1.28	0.59	0.6	4.28	19.27	5.6	4.33
7th (%)	1.85	0.79	0.64	0.17	4.59	19.28	11.76	2.52
11th (%)	0.52	0.81	1.14	1.7	4.47	27.63	27.38	21.93
13th (%)	0.77	0	1.9	0.62	5.12	27.76	20.15	36.86
17th (%)	2.95	11.36	13.68	12.79	18.08	14.91	13.2	2.903
19th (%)	9.21	20.04	25.74	26.52	18.9	3.51	17.85	6.28
23rd (%)	24.43	24.83	24.46	25.29	22.8	8.52	10.92	2.77
25th (%)	22.39	15.4	11.35	10.37	11.67	3.51	9.4	39.79
29th (%)	9.25	0.45	2.94	2.63	1.2	8.33	14.78	14.05
31st (%)	2.32	0.9	2.4	0.57	3.22	3.7	2.88	6.53
35th (%)	0.55	3.32	5.75	1.35	11.14	4.13	1.38	18.77
37th (%)	0.45	8.74	12.71	10.35	6.49	12.87	8.22	1.5
THD (%)	47.72	49.36	51.53	51.86	46.86	59.93	54.29	74.8

3.4 Filter sizing investigation

The LC filter is used to filter out the harmonics of the PWM current i_w to make the injected current i_s meet the grid codes. The size of the LC filter is determined by the harmonic performance of i_w. The previous section mentioned that different modulation schemes have different harmonic performance. Therefore, the size of the LC filter under different modulation schemes is different. This section discusses the performance of different modulation schemes in the filter sizing and the best modulation will be selected.

3.4.1 Filter design

Fig. 3-16 shows a simplified circuit of the grid-connected CSC for LC filter design, in which the transformer is omitted. R_f is the line resistance, L_f is the grid-side inductance, and C_f is the filter

capacitor. L_f usually comes from the leakage inductance of the transformer so the design of the LC filter mainly lies in the design of the filter capacitor C_f. The filter performance can be changed by changing the size of C_f.

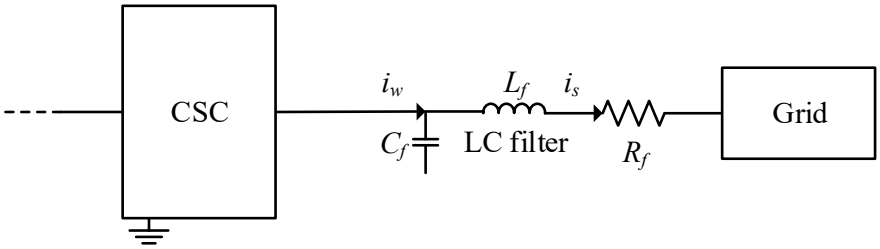

Fig. 3-16 Simplified circuit of the grid-connected CSC for LC filter design.

The transfer function of the LC filter is shown in (3-7):

$$\frac{i_s(j\omega)}{i_w(j\omega)} = \frac{1}{(j\omega)^2 L_f C_f + (j\omega) R_f C_f + 1} \tag{3-7}$$

where w is the angular frequency (for example, the angular frequency of the 5th harmonic is about 1885 rad/s).

The grid codes have requirements on both total harmonic distortion (THD) and individual harmonics of the grid-connected current i_s. Therefore, the LC filter should be sizing in a way that all harmonics should meet the grid codes [41]. For example, substitute the angular frequency of the 5th harmonic, the line resistance R_f, grid-side inductance L_f, the harmonic content $i_w(jw)$, and the standard value $i_s(jw)$ into the above formula, the minimum filter capacitance C_f required for this harmonic is obtained. The minimum filter capacitors can be obtained for the 7th, 11th, etc., in the same manner. The maximum of these minimums is selected as the final filter capacitance of the CSC.

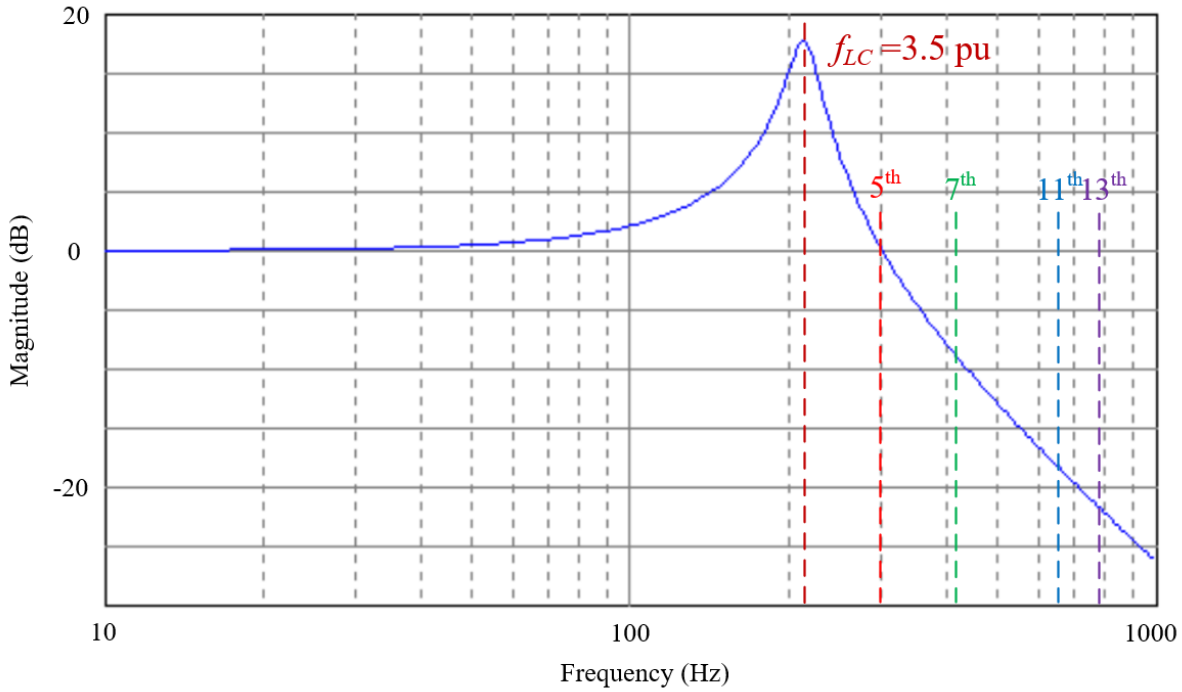

Fig. 3-17 Bode plot for the LC filter in SQ1.

Table 3-7 lists the minimum filter capacitors under individual harmonics. It is found that the C_f under SQ1 is the smallest, which is 0.79pu. The bode plot of this LC filter is shown in Fig. 3-17, where the cut-off frequency of the LC filter is about 3.5 pu.

Table 3-7 Filter Capacitance Calculation

Harmonic order	5	7	11	13	17	19	23	25	29	31	35	37
Standard i_s (%)	4	4	2	2	1.5	1.5	0.6	0.6	0.6	0.6	0.3	0.3
SQ1												
i_w (%)	0.59	0.64	1.14	1.9	13.7	25.7	24.5	11.4	2.94	2.4	5.75	12.7
C_f (pu)	0	0	0	0	0.35	0.5	0.79	0.32	0.07	0.05	0.16	0.32
SQ2												
i_w (%)	0.6	0.17	1.7	0.62	12.8	26.5	25.3	10.4	2.63	0.57	1.35	10.4
C_f (pu)	0	0	0	0	0.33	0.52	0.82	0.29	0.06	0	0.13	0.34
SQ3												
i_w (%)	4.28	4.59	4.47	5.12	18.1	18.9	22.8	11.7	1.2	3.22	11.1	6.49

C_f (pu)	0.83	0.44	0.27	0.21	0.45	0.38	0.74	0.33	0.04	0.07	0.31	0.17
SQ4												
i_w (%)	19.3	19.3	27.6	27.8	14.9	3.51	8.52	3.51	8.33	3.7	4.13	12.9
C_f (pu)	2.33	1.19	1.22	0.88	0.38	0.09	0.29	0.1	0.18	0.07	0.12	0.32
SQ5												
i_w (%)	5.6	11.8	27.4	20.2	13.2	17.9	10.9	9.4	14.8	2.88	1.38	8.22
C_f (pu)	0.96	0.8	1.21	0.66	0.34	0.36	0.36	0.27	0.3	0.06	0.05	0.21
SQ6												
i_w (%)	4.33	2.52	21.9	36.9	2.9	6.28	2.77	39.8	14.1	6.53	18.8	1.5
C_f (pu)	1.01	0	0.27	0.25	0.1	0.1	0.48	0.66	0.39	0.22	0.11	0.15
TPWM												
i_w (%)	4.57	1.85	0.52	0.77	2.95	9.21	24.4	22.4	9.25	2.32	0.55	0.45
C_f (pu)	0.86	0	0	0	0.1	0.2	0.79	0.61	0.2	0.05	0.02	0.02
SHE												
i_w (%)	1.28	0.79	0.81	0	11.4	20	24.8	15.4	0.45	0.9	3.32	8.74
C_f (pu)	0	0	0	0	0.3	0.4	0.8	0.4	0	0.03	0.11	0.22

3.4.2 Simulation results

Substituting the minimum filter capacitance C_f required by all the modulation schemes obtained in 3.4.1 into the simulation, the current i_s is obtained. i_s is a sinusoidal current that meets the grid code requirements and can be injected to the grid. Fig. 3-18 and Fig. 3-19 show the waveform and harmonic contents of i_s in SQ2 as an example. Since the fix-step size in simulation is limited, there are few harmonics around the third order in i_w. The LC filter will amplify these harmonics (as shown in Fig. 3-17, the resonance frequency is about 3.5 pu), the low-order harmonics of i_s (around 3rd order) are about 0.7% of fundamental, shown in Fig. 3-19.

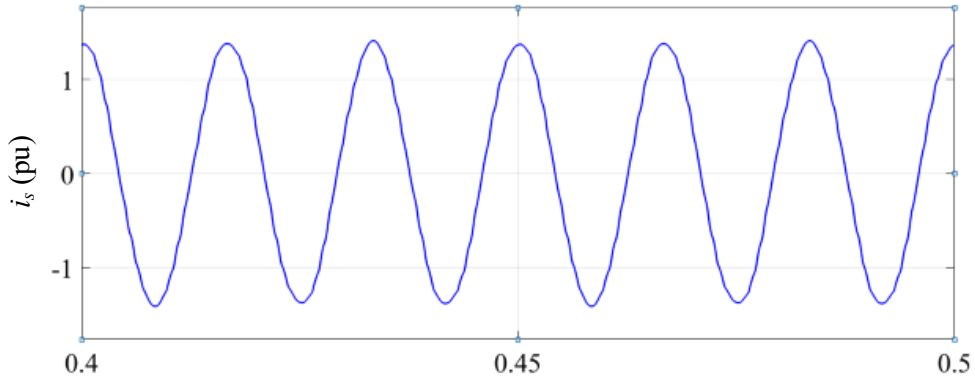

Fig. 3-18 Waveform of i_s in SQ2.

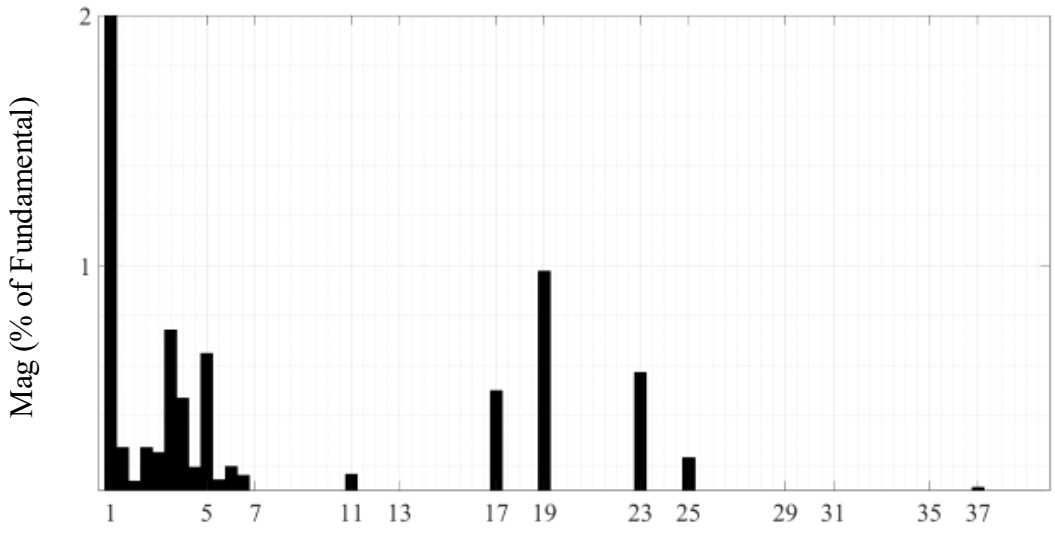

Fig. 3-19 Harmonics contents of i_s in SQ2.

3.5 Summary

The modulation schemes play an important role in the performance of the grid-side series-connected CSCs of the wind system. In addition to conventional performance in terms of DC current utilization, dynamic performance, digital implementation, harmonic performance, DC current bypass operation, and DC-link inductance, modulation schemes also affect the size of DC-link inductors.

This chapter is divided into the following parts: 1) Introducing the operation principle of all modulation schemes. 2) Analyzing and calculating the size of the required DC-link inductors in all the modulation schemes. 3) Analyzing the harmonic performance of all modulation schemes. 4) LC filter design for all modulation schemes.

The optimal modulation scheme should be SHE. As shown in Table 3-8 (n represents the number of CSCs connected in series), SHE has good harmonic performance, and the required DC-link inductance is relatively small. And most importantly, the required DC-link inductance of SHE is the smallest. This is the most critical because in grid-side series-connected CSCs of the wind system, the size of the DC-link inductor is multiplied, which is very bulky and costly.

Table 3-8 Investigated Performance of Different Modulation Schemes

Modulation Scheme	L_{dc} (pu)	C_f (pu)
SVM(SQ1)	$0.6n^2$	0.79*3n
SVM(SQ2)	$0.56n^2$	0.82*3n
SVM(SQ3)	$0.95n^2$	0.83*3n
SVM(SQ4)	$0.74n^2$	2.33*3n
SVM(SQ5)	$1.03n^2$	0.96*3n
SVM(SQ6)	$0.77n^2$	1.01*3n
SHE	$0.54n^2$	0.8*3n
TPWM	$0.77n^2$	0.86*3n

Chapter 4
Conclusions

This thesis presents a new PWM CSC-based offshore wind energy conversion system. The work mainly includes the new configuration, new control schemes, and the optimal modulation scheme investigation. This chapter summarizes contributions and conclusions, as well as future work.

4.1 Contributions and conclusions

The contributions and conclusions of this work are summarized as follows:

(1) A new PWM CSC-based offshore wind energy conversion system is proposed.

A new generator-side MFT-based power converter is proposed for the PWM CSC-based offshore wind system. Compared with the previous work, the proposed configuration can: 1) reduce the cost of power converters by using low-voltage and low-current switches, 2) facilitate the construction of HVDC using fewer turbine units by increasing the generator-side voltage gain, and 3) reduce the burden on MFT manufacturing by reducing its power rating.

(2) A new voltage/current balance control scheme is proposed for the proposed power converter.

The generator-side power converter of the proposed system has a hybrid connection structure including both series-connected and parallel-connected modules. In practice, due to component tolerances, the currents as well as voltages of the constituent modules are imbalanced. A voltage/current balance control scheme is proposed to solve this problem.

(3) Investigation on the optimal modulation scheme for the grid-side series-connected CSCs of the proposed system is conducted.

The optimal modulation scheme is investigated for the series-connected CSCs. The performance of different modulation schemes in terms of DC current utilization, dynamic performance, digital implementation, harmonic performance, DC current bypass operation, and DC-link inductance, is investigated. Finally, the optimal modulation scheme is recommended for the series-connected CSCs of the proposed wind system.

4.2 Future work

In the future, the following research work is suggested for the PWM CSC-based offshore wind energy conversion systems.

Optimal generator-side power converters

Power converters at the generator-side of the offshore wind energy conversion system are expected to feature 1) small size and weight, 2) low cost, 3) high reliability, and 4) good harmonics performance. However, existing power converters cannot ensure the above simultaneously. For example, the proposed one is with features of 1), 2), and 3), while it suffers a highly distorted generator current which is bad for the service lifespan of the generator. Therefore, innovative power converters ensuring all the above features are worth investigation.

References

[1] B. Wu, Y. Lang, N. Zargari and S. Kouro, Power Conversion and Control of Wind Energy Systems. Wiley-IEEE Press, 2011

[2] GWEC global wind report 2019. [online]. Available: https://gwec.net/global-wind-report-2019/#:~:text=Key%20findings%3A,per%20cent%20compared%20to%202018.

[3] ABB offshore wind connections. [Online]. Available: http://new.abb.com/systems/offshore-wind-connections.

[4] Siemens Gamesa Offshore pioneers. [Online]. Available: https://www.siemensgamesa.com/en-int/products-and-services/offshore

[5] P. Bresesti, W. L. Kling, R. L. Hendriks and R. Vailati, "HVDC Connection of Offshore Wind Farms to the Transmission System," in IEEE Transactions on Energy Conversion, vol. 22, no. 1, pp. 37-43, March 2007, doi: 10.1109/TEC.2006.889624.

[6] Z. Chen, J. M. Guerrero and F. Blaabjerg, "A Review of the State of the Art of Power Electronics for Wind Turbines," in IEEE Transactions on Power Electronics, vol. 24, no. 8, pp. 1859-1875, Aug. 2009, doi: 10.1109/TPEL.2009.2017082.

[7] Q. Wei, B. Wu, D. Xu and N. R. Zargari, "A Medium-Frequency Transformer-Based Wind Energy Conversion System Used for Current-Source Converter-Based Offshore Wind Farm," in IEEE Transactions on Power Electronics, vol. 32, no. 1, pp. 248-259, Jan. 2017, doi: 10.1109/TPEL.2016.2524635.

[8] Q. Wei, B. Wu, D. Xu and N. R. Zargari, "A New Configuration Using PWM Current Source Converters in Low-Voltage Turbine-Based Wind Energy Conversion Systems," in IEEE Journal of Emerging and Selected Topics in Power Electronics, vol. 6, no. 2, pp. 919-929, June 2018, doi: 10.1109/JESTPE.2017.2748281.

[9] M. Popat, B. Wu, F. Liu and N. Zargari, "Coordinated Control of Cascaded Current-Source Converter Based Offshore Wind Farm," in IEEE Transactions on Sustainable Energy, vol. 3, no. 3, pp. 557-565, July 2012, doi: 10.1109/TSTE.2012.2191986.

[10] T. H. Nguyen, D. Lee and C. Kim, "A Series-Connected Topology of a Diode Rectifier and a Voltage-Source Converter for an HVDC Transmission System," in IEEE Transactions on Power Electronics, vol. 29, no. 4, pp. 1579-1584, April 2014, doi: 10.1109/TPEL.2013.2283368.

[11] G. Guo et al., "HB and FB MMC Based Onshore Converter in Series-Connected Offshore Wind Farm," in IEEE Transactions on Power Electronics, vol. 35, no. 3, pp. 2646-2658, March 2020, doi: 10.1109/TPEL.2019.2929689.

[12] N. Holtsmark, H. J. Bahirat, M. Molinas, B. A. Mork and H. K. Hoidalen, "An All-DC Offshore Wind Farm With Series-Connected Turbines: An Alternative to the Classical Parallel AC Model?," in IEEE Transactions on Industrial Electronics, vol. 60, no. 6, pp. 2420-2428, June 2013, doi: 10.1109/TIE.2012.2232255.

[13] G. Guo et al., "Series-Connected-Based Offshore Wind Farms With Full-Bridge Modular Multilevel Converter as Grid- and Generator-side Converters," in IEEE Transactions on Industrial Electronics, vol. 67, no. 4, pp. 2798-2809, April 2020, doi: 10.1109/TIE.2019.2912777.

[14] M. Popat, B. Wu and N. R. Zargari, "A Novel Decoupled Interconnecting Method for Current-Source Converter-Based Offshore Wind Farms," in IEEE Transactions on Power Electronics, vol. 27, no. 10, pp. 4224-4233, Oct. 2012, doi: 10.1109/TPEL.2012.2191982.

[15] Q. Wei, B. Wu, D. Xu and N. R. Zargari, "Bipolar Operation Investigation of Current Source Converter Based Wind Energy Conversion Systems," in IEEE Transactions on Power Electronics, vol. 33, no. 2, pp. 1294-1302, Feb. 2018, doi: 10.1109/TPEL.2017.2683262.

[16] Q. Wei, B. Wu, D. Xu and N. R. Zargari, "An Optimized Strategy for PWM Current Source Converter Based Wind Conversion Systems With Reduced Cost and Improved Efficiency," in IEEE Transactions on Power Electronics, vol. 33, no. 2, pp. 1202-1210, Feb. 2018, doi: 10.1109/TPEL.2017.2676106.

[17] A. Garcés and M. Molinas, "A Study of Efficiency in a Reduced Matrix Converter for Offshore Wind Farms," in IEEE Transactions on Industrial Electronics, vol. 59, no. 1, pp. 184-193, Jan. 2012, doi: 10.1109/TIE.2011.2130502.

[18] E. Veilleux and P. W. Lehn, "Interconnection of Direct-Drive Wind Turbines Using a Series-Connected DC Grid," in IEEE Transactions on Sustainable Energy, vol. 5, no. 1, pp. 139-147, Jan. 2014, doi: 10.1109/TSTE.2013.2276616.

[19] V. Yaramasu, B. Wu, P. C. Sen, S. Kouro and M. Narimani, "High-power wind energy conversion systems: State-of-the-art and emerging technologies," in Proceedings of the IEEE, vol. 103, no. 5, pp. 740-788, May 2015, doi: 10.1109/JPROC.2014.2378692.

[20] R. Blasco-Gimenez, N. Aparicio, S. Ano-Villalba and S. Bernal-Perez, "LCC-HVDC Connection of Offshore Wind Farms With Reduced Filter Banks," in IEEE Transactions on Industrial Electronics, vol. 60, no. 6, pp. 2372-2380, June 2013, doi: 10.1109/TIE.2012.2227906.

[21] R. Li, S. Bozhko and G. Asher, "Frequency Control Design for Offshore Wind Farm Grid With LCC-HVDC Link Connection," in IEEE Transactions on Power Electronics, vol. 23, no. 3, pp. 1085-1092, May 2008, doi: 10.1109/TPEL.2008.921193.

[22] S. Bernal-Perez, S. Ano-Villalba, R. Blasco-Gimenez and J. Rodriguez-D'Derlee, "Efficiency and Fault Ride-Through Performance of a Diode-Rectifier- and VSC-Inverter-Based HVDC Link for Offshore Wind Farms," in IEEE Transactions on Industrial Electronics, vol. 60, no. 6, pp. 2401-2409, June 2013, doi: 10.1109/TIE.2012.2222855.

[23] M. Amin and M. Molinas, "A Gray-Box Method for Stability and Controller Parameter Estimation in HVDC-Connected Wind Farms Based on Nonparametric Impedance," in IEEE Transactions on Industrial Electronics, vol. 66, no. 3, pp. 1872-1882, March 2019, doi: 10.1109/TIE.2018.2840516.

[24] E. Agheb and H. K. Høidalen, "Medium frequency high power transformers, state of art and challenges," 2012 International Conference on Renewable Energy Research and Applications (ICRERA), Nagasaki, 2012, pp. 1-6, doi: 10.1109/ICRERA.2012.6477318.

[25] S. Vaisambhayana, C. Dincan, C. Shuyu, A. Tripathi, T. Haonan and B. R. Karthikeya, "State of art survey for design of medium frequency high power transformer," 2016 Asian Conference on Energy, Power and Transportation Electrification (ACEPT), Singapore, 2016, pp. 1-9, doi: 10.1109/ACEPT.2016.7811550.

[26] M. Mogorovic and D. Dujic, "100 kW, 10 kHz Medium-Frequency Transformer Design Optimization and Experimental Verification," in IEEE Transactions on Power Electronics, vol. 34, no. 2, pp. 1696-1708, Feb. 2019, doi: 10.1109/TPEL.2018.2835564.

[27] J. Dai, D. Xu, B. Wu and N. R. Zargari, "Unified DC-Link Current Control for Low-Voltage Ride-Through in Current-Source-Converter-Based Wind Energy Conversion Systems," in IEEE Transactions on Power Electronics, vol. 26, no. 1, pp. 288-297, Jan. 2011, doi: 10.1109/TPEL.2010.2059377.

[28] B. Wu, High-Power Converters and AC Drives. New York, NY, USA/Piscataway, NJ, USA: Wiley/IEEE Press, 2006.

[29] Y. W. Li, B. Wu, D. Xu, and N. R. Zargari, “Space vector sequence investigation and synchronization methods for active front-end rectifiers in high-power current-source drives,” IEEE Transactions on Industrial Electronics, vol. 55, no. 3, pp. 1022–1034, Mar. 2008.

[30] Q. Wei, B. Wu, D. D. Xu and N. R. Zargari, "Optimal Space Vector Sequence Investigation Based on Natural Sampling SVM for Medium-Voltage Current-Source Converter," in IEEE Transactions on Power Electronics, vol. 32, no. 1, pp. 176-185, Jan. 2017.

[31] D. G. Holmes, "A unified modulation algorithm for voltage and current source inverters based on AC-AC matrix converter theory," in IEEE Transactions on Industry Applications, vol. 28, no. 1, pp. 31-40, Jan.-Feb. 1992, doi: 10.1109/28.120210.

[32] D. N. Zmood and D. G. Holmes, "A generalised approach to the modulation of current source inverters," PESC 98 Record. 29th Annual IEEE Power Electronics Specialists Conference (Cat. No.98CH36196), Fukuoka, 1998, pp. 739-745 vol.1, doi: 10.1109/PESC.1998.701981.

[33] O. Ojo and S. Vanaparthy, "Carrier-based discontinuous PWM modulation for current source converters," Conference Record of the 2004 IEEE Industry Applications Conference, 2004. 39th IAS Annual Meeting., Seattle, WA, USA, 2004, pp. 2224-2231 vol.4, doi: 10.1109/IAS.2004.1348785.

[34] T. Halkosaari and H. Tuusa, "Optimal vector modulation of a PWM current source converter according to minimal switching losses," 2000 IEEE 31st Annual Power Electronics Specialists Conference. Conference Proceedings (Cat. No.00CH37018), Galway, Ireland, 2000, pp. 127-132 vol.1, doi: 10.1109/PESC.2000.878821.

[35] E. P. Wiechmann, R. P. Burgos and J. Holtz, "Active front-end converter for medium-voltage current-source drives using sequential-sampling synchronous space-vector modulation," in IEEE Transactions on Industrial Electronics, vol. 50, no. 6, pp. 1275-1289, Dec. 2003, doi: 10.1109/TIE.2003.819692.

[36] J. D. Ma, Bin Wu, N. R. Zargari and S. C. Rizzo, "A space vector modulated CSI-based AC drive for multimotor applications," in IEEE Transactions on Power Electronics, vol. 16, no. 4, pp. 535-544, July 2001, doi: 10.1109/63.931075.

[37] A. Moeini, H. Zhao and S. Wang, "A Current-Reference-Based Selective Harmonic Current Mitigation PWM Technique to Improve the Performance of Cascaded H-Bridge Multilevel Active Rectifiers," in IEEE Transactions on Industrial Electronics, vol. 65, no. 1, pp. 727-737, Jan. 2018, doi: 10.1109/TIE.2016.2630664.

[38] K. Yang, Q. Zhang, R. Yuan, W. Yu, J. Yuan and J. Wang, "Selective Harmonic Elimination With Groebner Bases and Symmetric Polynomials," in IEEE Transactions on Power Electronics, vol. 31, no. 4, pp. 2742-2752, April 2016, doi: 10.1109/TPEL.2015.2447555.

[39] H. Zhao, T. Jin, S. Wang and L. Sun, "A Real-Time Selective Harmonic Elimination Based on a Transient-Free Inner Closed-Loop Control for Cascaded Multilevel Inverters," in IEEE Transactions on Power Electronics, vol. 31, no. 2, pp. 1000-1014, Feb. 2016, doi: 10.1109/TPEL.2015.2413898.

[40] D. Xu and B. Wu, "Multilevel Current Source Inverters with Phase Shifted Trapezoidal PWM," 2005 IEEE 36th Power Electronics Specialists Conference, Recife, 2005, pp. 2540-2546, doi: 10.1109/PESC.2005.1581990.

[41] Q. Wei, B. Wu, D. Xu and N. R. Zargari, "Minimization of Filter Capacitor for Medium-Voltage Current-Source Converters Based on Natural Sampling SVM," in IEEE Transactions on Power Electronics, vol. 33, no. 1, pp. 473-481, Jan. 2018, doi: 10.1109/TPEL.2017.2663779.